TWENTY FIRST EUROPEAN ROTORCRAFT FORUM

Paper No. I-7

KEY RESULTS FROM A HIGHER HARMONIC CONTROL AEROACOUSTIC ROTOR TEST (HART) IN THE GERMAN-DUTCH WIND TUNNEL

W. R. Splettstoesser, R. Kube, U. Seelhorst, W. Wagner,
DLR BRAUNSCHWEIG AND GÖTTINGEN
GERMANY

A. Boutier, F. Micheli
ONERA, CHATILLON
FRANCE

E. Mercker, K. Pengel
DNW, EMMELOORD
THE NETHERLANDS

August 30 - September 1, 1995

SAINT-PETERSBURG, RUSSIA

Paper nr.: I.7

Key Results from a Higher Harmonic Control Aeroacoustic Rotor Test (Hart) in the German-Dutch Wind Tunnel.

W.R. Splettstoesser; R. Kube; U. Seelhorst; W. Wagner; A. Boutier; F. Micheli; E. Mercker; K. Pengel

TWENTY FIRST EUROPEAN ROTORCRAFT FORUM
August 30 - September 1, 1995 Saint-Petersburg, Russia

KEY RESULTS FROM A HIGHER HARMONIC CONTROL AEROACOUSTIC ROTOR TEST (HART) IN THE GERMAN-DUTCH WIND TUNNEL

W. R. Splettstoesser, R. Kube, W. Wagner, U. Seelhorst
DLR Braunschweig and Göttingen, Germany

A. Boutier, F. Micheli
ONERA, Chatillon, France

E. Mercker, K. Pengel
DNW, Emmeloord, The Netherlands

ABSTRACT

In a major cooperative research program within existing US-German and US-French Memoranda of Understandings (MoU's) a comprehensive experimental study was conducted with a 40-percent geometrically and dynamically scaled BO-105 main rotor operated in the open-jet anechoic test section of the German-Dutch Wind Tunnel (DNW). The objectives of the program were to improve the physical understanding and the mathematical modelling of the effects of the higher harmonic blade pitch control technique on blade-vortex interaction (BVI) impulsive noise and vibration reduction. A unique set of acoustic, aerodynamic, dynamic response, performance, and rotor wake data were acquired with a pressure and strain gauge instrumented blade and by application of non-intrusive measurement techniques. This paper is focused on the experimental part of this research program, termed Higher-harmonic-control Aeroacoustic Rotor Test (HART) which was jointly performed by researchers from the US-Army Aeroflightdynamics Directorate (AFDD) and NASA Langley, the DNW, and the French and German Aerospace Research Establishments ONERA and DLR. The test procedures applied and key results obtained are presented.

SYMBOLS

a_o	freestream speed of sound, m/s
BL	baseline case (no HHC)
C_N	sectional normal force coefficient (blade section axis) $(dN/dr)/q_r(r,\psi)c$
C_p	pressure coefficient $(P-P_o)/q_r(r,\psi)$
C_T	rotor thrust coefficient, thrust$/\rho_o \pi R^2 (\Omega R)^2$
c	blade chord, m
f	frequency, 1/s
f_{bp}	blade passage frequency, 1/s
GF	vibration quality criterion, rms value of 4-per-rev components of balance forces and moments, normalized to baseline (no HHC) GF, %
L-MF	mid-frequency bandpass noise level (6th - 40th f_{bp} harmonic, 30 averages), dB
L-LF	low-frequency bandpass noise level (2nd - 5th f_{bp} harmonic, 30 averages), dB
M_H	hover tip Mach number, $\Omega R/a_o$
MN	minimum noise HHC case
MV	minimum vibration HHC case
nP	n'th harmonic of rotational period
P_o	freestream static pressure, N/m^2
$q_r(r,\psi)$	relative dynamic pressure, $0.5\ \rho_o (\Omega r + V_T \sin\psi)^2$, N/m^2
R	rotor Radius, m
r	radial distance from hub, m
r_v	tip vortex core radius, m
U	velocity component in X-direction, m/s
V	velocity component in Y-direction, m/s
V_T	freestream (tunnel) flow velocity, m/s
W	velocity component in Z-direction, m/s
X	streamwise coordinate relative to hub, positive downstream, m
Y	cross-flow coordinate relative to hub, positive on advancing side, m
Z	vertical cross-flow coordinate relative to hub, positive above hub, m
α	rotor tip path plane angle referenced to tunnel streamwise axis, positive for backward tilt, deg
α'	effective α corrected for open-jet wind tunnel effect, deg
α_s	rotor shaft angle, deg
Γ	tip vortex circulation (vortex strength), m^2/s
θ	pitch angle of blade at ψ, deg
θ_c	amplitude of higher harmonic pitch at ψ_c, deg
θ_{fp}	calculated "full-scale helicopter" flight path angle,positive in descent, deg
ϕ	HHC system phase angle, referenced to positive θ_c for reference blade passing zero azimuth (ψ=0), deg
μ	advance ratio, $V_T/\Omega R$
ρ_o	freestream air density, kg/m^3
ψ	blade azimuth angle, deg
ψ_c	blade azimuth angle corresponding to θ_c, see Fig. 4, deg
Ω	rotor rotational speed, rad/s

Presented at the 21st European Rotorcraft Forum
Saint-Petersburg, Russia, August 30 - September 1, 1995 I.7-1

INTRODUCTION

Helicopter rotor noise and particularly blade-vortex interaction (BVI) impulsive noise is considered a matter of major concern for the acceptability of rotorcraft in densely populated areas. This impulse type noise is very annoying since it dominates the noise radiation in the mid-frequency range to which human subjective response is most sensitive. BVI noise is caused by the highly unsteady aerodynamic interaction of a rotor blade with the vortex system shed by preceding blades. This phenomenon is generally observed during partial power descent, especially during landing approach, and at maneuver flight condition, when the miss distance between the rolled-up tip vortices and the rotor plane becomes extremely small.

More than one decade ago, experimental studies on BVI noise were conducted on in-flight full-scale and model-scale helicopter rotors in order to establish the operational envelope for BVI occurrence (Ref. 1-3), the primary parameters for BVI noise generation and radiation, and the model-to-full-scale acoustic scaling conditions (Refs. 4-6). Advancing and retreating side BVI noise sources were localized in the first and fourth quadrant of the rotor plane with maximum intensities where blade and vortex axis were close to parallel, Refs. (7, 8). More recent research work in Europe and the US have demonstrated a potential for significant reduction of BVI noise and vibrations by application of higher harmonic (multicyclic) pitch control techniques. Originally, higher harmonic control (HHC) was developed to improve the helicopter ride quality and the reduction of vibration levels up to 90-percent was demonstrated (Ref. 9).

A potential benefit of the HHC concept for BVI noise reduction was suggested in the late 80's and subsequently pursued and tested (Refs. 10-12). The noise reduction hypothesis of Ref. 10, sketched in Fig. 1, stated that attenuation of local blade lift, tip vortex strength, and/or enlargement of blade-vortex miss distance at the BVI encounters should help to reduce the BVI effect on the unsteady airloads and thus on noise. Initial results (Ref. 11) indicated a noise reduction potential of about 5 to 6dBA of the maximum BVI noise level, however, at the cost of increased low frequency loading noise. Similar results and trends were observed during a flight test program on active vibration control on an experimental SA 349 Gazelle helicopter (Ref. 12). During the first systematic wind tunnel programs in the Transonic Dynamic Tunnel (TDT) of NASA Langley (Ref. 13) and in the DNW (Refs. 14, 15) noise reduction potentials of about 6dB of the maximum mid-frequency (BVI) noise level were demonstrated. Also, it was realized that at HHC schedules, most beneficial for BVI noise reduction, low frequency noise and vibrational loads were increased. Only few HHC schedules were found, for which both BVI noise and vibrations could be reduced.

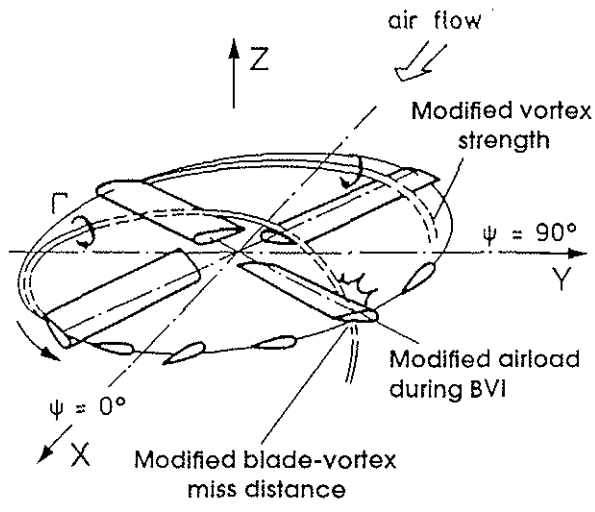

Fig. 1 Illustration of the BVI noise reduction concept.

In order to develop a better understanding of the physics behind these phenomena and to demonstrate the benefit of active rotor control techniques like HHC or IBC (individual blade control) a major basic research effort was initiated. Under the auspices of existing US/German and US/French Memoranda of Understanding (MoU's) for cooperative research in the field of Helicopter Aeromechanics, the Higher-harmonic-control Aeroacoustic Rotor Test (HART) program was launched in 1990. Other existing bilateral or national cooperation agreements between DLR/NLR, ONERA/DLR, DLR/NASA, and US-Army/NASA have been very supportive.

This paper is focused on the experimental part of this joint research program, which created a comprehensive set of acoustic, aerodynamic, blade dynamic, rotor performance and rotor wake data for rotor operation without and with different HHC inputs. The test procedures and measurement techniques applied are briefly documented and key results are presented. Some of the important results have been further analysed for better understanding of the physics behind the observed significant changes of BVI noise generation when HHC inputs are varied.

HART OBJECTIVES AND APPROACH

The program objectives were to develop and improve the physical understanding and the mathematical modeling of the effects of higher harmonic blade pitch control on blade-vortex interaction (BVI) noise and vibration. This included theoretical and experimental research into the related aerodynamic and acoustic phenomena creating rotor impulsive noise and vibration.

From previous analytical and experimental work, the following parameters were identified to control BVI noise and vibration: local blade lift distribution, tip vortex

geometry, tip vortex strength and core size, blade-vortex miss distance, and aeroelastic blade deflections. Between the partners a combined analytical and experimental approach have been agreed to analyse, predict, and measure these parameters. Consequently, the main features of the approach were (1) to evaluate existing test data, (2) to develop or improve analytical codes for rotor aerodynamics and acoustics including multicyclic pitch variations, and (3) to generate an experimental data base for code validation and for exploration of the physics behind the phenomena. The work was organized by two teams, the prediction team and the test team (Refs. 16, 17).

The test team, coordinated by DLR, was formed with scientists from DLR, ONERA, NASA Langley, US-Army AFDD, and the DNW. The test team was responsible for preparing and conducting the test in the DNW. Based on analytical studies and pre-test predictions (Ref. 18), the prediction team contributed to the definition of the test matrix and of the parameters to be measured. Jointly, a test plan was generated pertaining to the measurement of (1) acoustic radiation with a movable microphone array, (2) blade surface pressures with absolute pressure transducers, (3) tip vortex geometry segments and blade-vortex miss distance with a Laser Light Sheet (LLS) flow visualization technique, (4) vortex strength and core size with a Laser Doppler Velocimeter (LDV), (5) blade deflections with a Projected Grid Method (PGM) and with strain gauges placed on the rotor, and (6) blade tip altitude and deflections with a Target Attitude in Real Time (TART) method. Some of these non-intrusive measurement techniques (e.g. PGM) have specifically been developed for this test. Other techniques (e.g. LDV) had to be improved with respect to extended measurement range and/or 3D capability and had to prove its functionality during wind tunnel pre-tests (Refs. 19, 20).

TEST PROGRAM

Details of the instrumented model rotor, the data acquisition systems for rotor, acoustic and aerodynamic blade pressure data are given in Ref. 21. Some important features are reported here.

Test Set-up

The experimental program was conducted in the open-jet, anechoic test section of the DNW. The open-jet configuration employed an 8m by 6m nozzle that provides a 19m-long free jet with a low-turbulence potential core. In Fig. 2, the DLR model rotor test stand mounted on the DNW sting is shown together with the traversing in-flow microphone array which was placed 2.3m underneath. The test stand fuselage, sting and traverse were acoustically treated to minimize reflections. The rotor hub was positioned 7m downstream from the nozzle exit and 1m above tunnel center. The test rig essentially consisted of a support mounted 6-component balance, measuring both the static and dynamic rotor forces and moments. On the same support a hydraulic motor was mounted to drive the rotor shaft via a flexible belt. By this arrangement a hollow rotor shaft was provided for the instrumentation

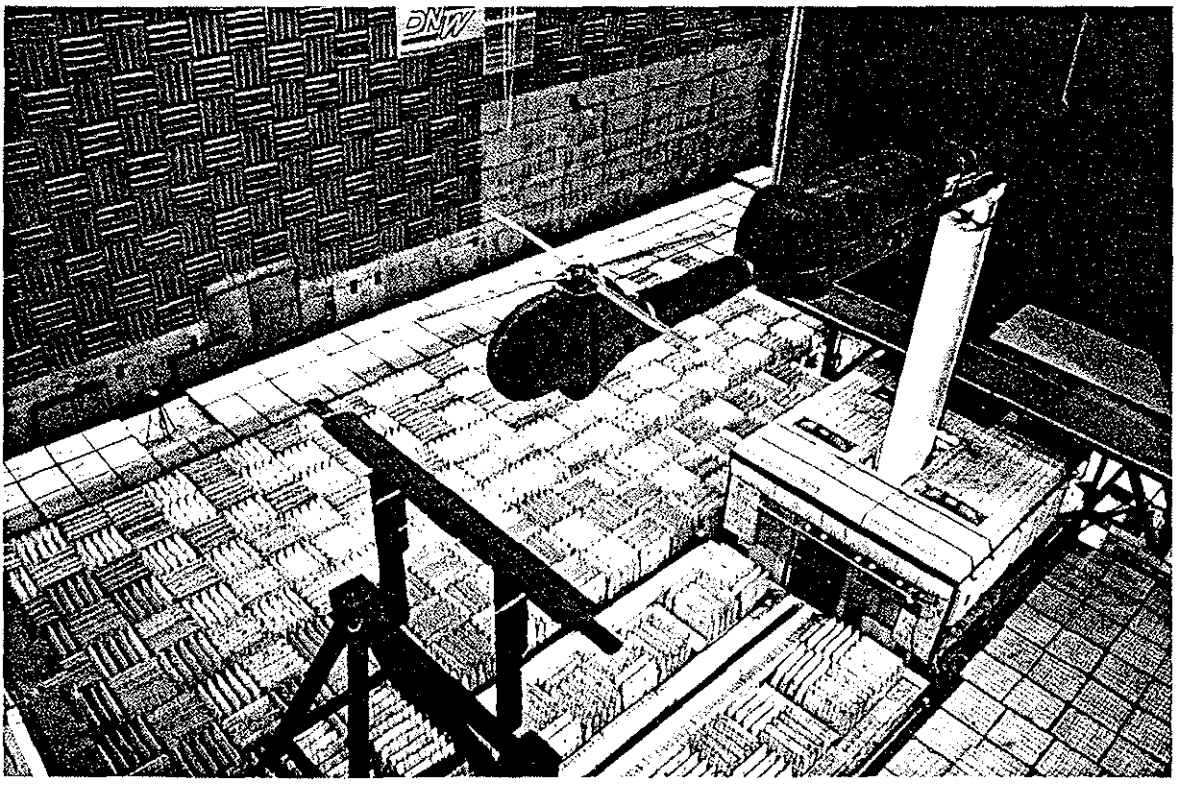

Fig. 2 Model rotor and in-flow microphone traverse in the DNW open test section.

cabling of the rotating system. The four-bladed hingeless rotor was a 40-percent, dynamically and Mach-scaled model of the BO-105 main rotor. The 4m-diameter rotor had 121mm chord, NACA 23012 section blades with -8° linear twist and standard rectangular tips. One of the blades was densely instrumented with 124 subminiature pressure transducers of the piezoresistive type (distribution shown in Fig. 3) and 32 strain gauges. Like all other signals of the rotating frame, the sensor output signals were fed through the rotor shaft into a computer controlled miniature amplifier unit for proper pre-amplification before transmission to the fixed frame via a slipring assembly.

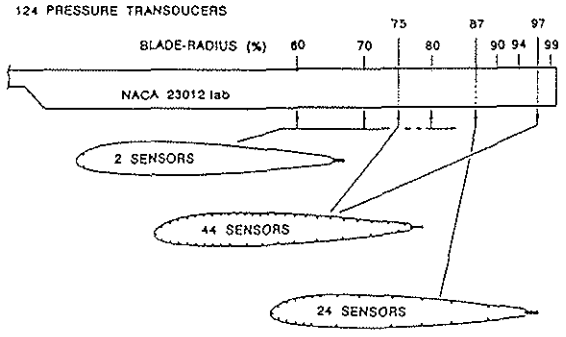

Fig. 3 Pressure transducer distribution

Rotor Operation

The rotor was controlled by three electro-hydraulic actuators below the swashplate which had a high cut-off frequency and therefore featured HHC capabilities. For this 4-bladed rotor, the higher harmonic pitch was achieved by superimposing 4P (4-per-revolution) swashplate motion upon the basic swashplate collective and cyclic (1P) flight control inputs. Collective 4P pitch motion (all 4 blades pitching simultaneously the same way) was provided as well as pitch schedules containing 3P and 5P pitch components, through proper phasing the 4P swashplate inputs. For this HART test transputer based manual HHC input was used allowing an easy and time efficient variation of the HHC amplitude and phase shift. The pitch motion achieved and the rotor operation can be explained on the basis of Fig. 4, which shows blade pitch angle θ versus rotor azimuth angle ψ for a specific simulated flight condition. For a given advance ratio μ and tip-path-plane angle α, a mean collective of 6° for the required C_T and a basic 1P pitch of 2.1° for zero flapping trim were used as illustrated.

Once performance and aeroacoustic data were acquired for the baseline case, pre-selected HHC pitch was superimposed to generate a pitch deflection of θ_c at azimuth ψ_c and data were taken again. Since only minor variations in thrust coefficient and rotor trim were observed, no adjustments were necessary in mean collective and cyclic pitch. The net higher harmonic portion (difference of total

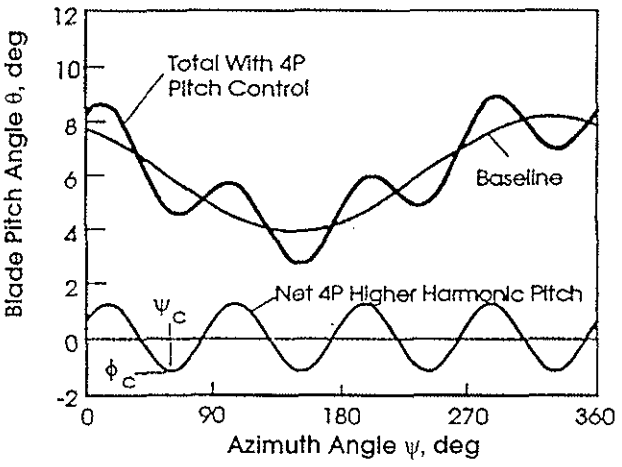

Fig. 4 Superposition principle of higher harmonic blade pitch.

and baseline case pitch) is illustrated in Fig. 4 for a 4P HHC case. For the 3P aeroacoustic data presented in this report, HHC amplitude θ_c and azimuth angle ψ_c ($0 \le \psi_c < 120°$) were obtained from the 3P components (amplitude and phase) of the measured pitch angle FFT analysis. Similar considerations are valid for 4P and 5P pitch schedules with definition of the azimuth angle ranges of $0 \le \psi_c < 90°$ and $0 \le \psi_c < 72°$, respectively.

Acoustic and Blade Pressure Measurements

The emitted rotor noise was measured by eleven movable and three stationary 1/2-inch microphones of the pressure response type mounted with nose cones. The movable microphones of the in-flow array were arranged symmetrically and spaced 0.54m apart on a horizontal wing (Fig. 2). The array was traversed 4m upstream and 4m downstream of the rotor hub (X-direction) creating a large horizontal measurement plane (X/R=4, Y/R=2.7) at a distance of Z/R=1.15 underneath the rotor hub. One of the stationary microphones was mounted on the advancing side of the fuselage 0.6R below the hub, the other two were installed on either side of the nozzle exit within the rotor plane. From the slowly moving (33mm/s) microphone array 30 rotor revolutions of microphone data were taken by a transputer based system at each streamwise step, 0.5m apart. After completion of a traverse the sound field was defined by 187 individual measurement points providing an excellent spatial resolution. The 30 rotor revolutions, at 2048 samples per revolution of real-time acoustic pressure data were processed on-line as well as being stored for further analysis. Bandpass filtering was used so that the useful frequency range was 20Hz to 18kHz. In addition to standard system calibrations, background noise and acoustic quality tests were performed. The acoustic data were evaluated in terms of mid-frequency band pass levels (L-MF) comprising the 6th - 40th blade passage frequency harmonics (a representative measure for BVI impulsive noise) and in terms of low-frequency

levels (L-LF) comprising the 2nd - 5th harmonic (a measure for low frequency loading noise).

A similar transputer based system with a capacity of 230 channels was used for the acquisition of the blade pressure and strain gauge data. Each of these channels was digitized at a rate of 2048 per revolution providing a useful frequency range up to 18kHz, however, due to the specifics of the pressure transducers and their installation a flat frequency response up to 7kHz have been proven, which is more than sufficient for the blade pressure signals. For each rotor condition 64 revolutions were sampled immediately before each microphone traverse was started and on-line processed during the acoustic data acquisition.

The data acquisition was initiated when wind tunnel and rotor were reported on condition. After acquisition of the wind tunnel data and shortly before the acquisition of the blade pressure data, the rotor data were measured over a period of 32 revolutions; 96 sensor signals were digitized at 128 samples per revolution with a useful frequency content of 210Hz (12P). All data acquisition systems were triggered by blade position reference signals from an angle encoder. Digitized wind tunnel and rotor data were merged into a common data base.

Laser Light Sheet Flow Visualization

The Laser Light Sheet (LLS) technique (Ref. 22) was chosen (1) to visualize tip vortex sections in order to gain some qualitative information on the vortex structure inclusive the vortex core center and (2) to attain quantitative information on the geometry of tip vortex segments and on the blade-vortex miss distance at locations near severe BVI. The set-up is illustrated in Fig. 5. A laser light sheet was erected normal to the rotor plane and approximately vertical to the vortices to be visualized. It was emitted by an optical package (powered by a 5W Argon-ion laser) which was mounted on the microphone traverse such that the light sheet could easily be moved. In order to visualize a vortex section cut by the light sheet an oil aerosol had to be introduced at the blade tip at that azimuth where this vortex element was generated. For this purpose a remotely controlled traversable oil smoke generator was mounted on top of the wind tunnel nozzle. When the smoke probe was correctly adjusted, the smoke particles within the vortex section were illuminated by the high intensity laser light and the vortex structure became visible, such that the vortex core center could be identified. The scattered light was recorded by a fast motion video camera, mounted as shown on top of the nozzle and triggered by a 512-per-revolution signal of the rotor.

A further objective of the LLS test was to determine the distance of the tip vortices with respect to a passing rotor

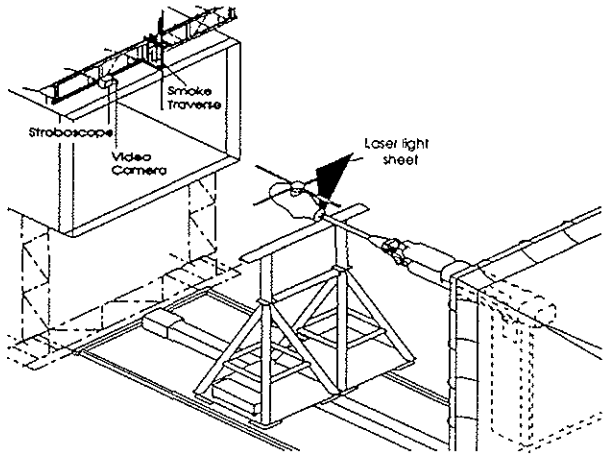

Fig. 5 LLS Flow visualization test set-up.

blade at the azimuth near or at the interaction. Therefore it was necessary to visualize the vortex and the respective blade simultaneously, a requirement that was accomplished by means of a powerful stroboscopic light source. It was installed in the proximity of the video camera and, like this, was synchronized with the blade azimuth via the same 512-per-revolution signal. In order to quantify the locations of both the vortex core center and the blade, referenced to the rotor hub, a reference grid of known dimensions was placed in the plane of the light sheet (after the wind and the rotor had stopped) and was recorded with the same video camera. Later on, this video recording was digitized and superimposed on the original video image, thus allowing to quantify the locations (X, Y, Z) of the vortex core center and of the blade (the intersection of leading edge and light sheet); ΔZ then represented an estimate for the blade-vortex miss distance. The third objective, the quantification of vortex segments was accomplished by repeated measurements of the vortex core center along a vortex line at a "frozen" vortex pattern, i.e. with the blade at a fixed azimuth angle.

Laser Doppler Velocimetry (LDV) Measurements

The objectives of the LDV measurements were to attain vortex strength (circulation) and core size of the vortices interacting intensively with the rotor blades on the advancing side near 46° azimuth and on the retreating side near 306°, respectively (known from pre-test predictions, Ref. 18). This was accomplished by measuring the vortex velocity fields by means of two LDV systems, simultaneously operated on the advancing side by DLR (LDV-1) and on the retreating side by ONERA (LDV-2). Both systems, placed on platforms of 9m height (Fig. 6), had a working distance of 5m and 3D capability, a necessary requirement for measurements in the rotor wake.

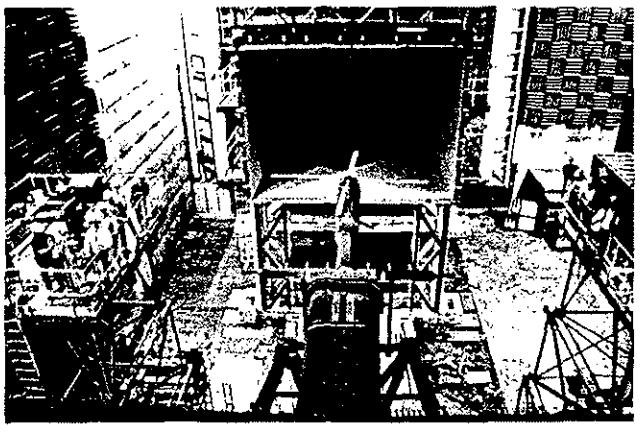

Fig. 6 Arrangement of LDV set-ups and rotor rig.

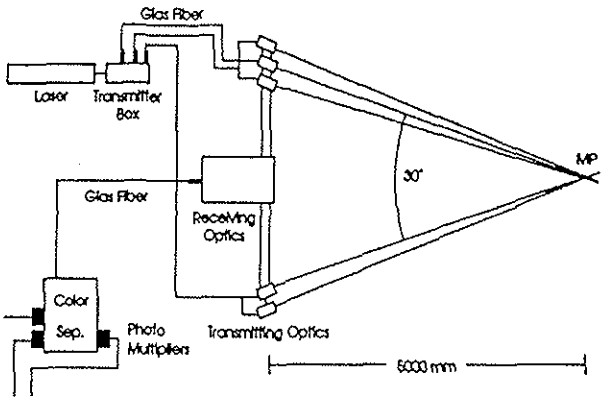

Fig. 7 Scheme of a 3D LDV system with 5m working range.

Flow seeding with oil aerosol (LDV-1) and incense smoke (LDV-2) was conducted by two independent, remotely controlled smoke generator systems installed about 50m upstream in the settling chamber; particle size was less than 1 μm . Both LDV systems operated in the back scatter, off-axis mode and used the most intensive laser light components of 476.5nm (violet), 488nm (blue), and 514.5nm (green) provided by all line Argon lasers of 6W power (LDV-1) and 10W plus 2W (LDV-2). The principle arrangement of the LDV systems is shown in Fig. 7 (Refs. 19, 20). Each of the laser beams was divided into two individual beams with similar intensity, one of them superimposed with a Bragg shift in the MHz range, to determine both velocity modulus and direction of each velocity component. The laser beams were coupled into single mode glass fibres and launched into the probe volume via individual transmitting optics. For high resolution of the velocity components and a well defined small probe volume, the optical axis of the emitting and receiving optics were arranged at an angle of $\pm 15°$ within the horizontal plane. The dimensions of the probe volumes were about 0.4mm diameter (LDV-2) and 0.25mm diameter and 1mm length (LDV-1). The back-scattered light of all three lines was collected by receiving optics (a concave mirror at LDV-1 and a Cassegrain telescope at LDV-2), fed into a colour separator before entering the photo multipliers. With this architecture similar beam intensities at the probe volume and a symmetry of the components relative to the main flow could be achieved, thus ensuring a high accuracy and an optimal velocity measurement domain.

The task of the LDV measurements was to determine the velocity field of the vortex under consideration within a square field about 2 by 2 chord lengths. Since spatial mapping was prohibitive due to time constraint, velocity time history measurements at different vertical displacements of the probe volume were chosen. In order to avoid any interference with a blade, the probe volumes were placed upstream of the BVI locations at about $\psi = 55°$ at r/R=0.75 and at $\psi = 298°$ at r/R=0.8 and an observation time window of 72ms corresponding to 45° rotor rotation was chosen, which was opened and closed for data acquisition before the blade arrived at the azimuth of the probe volume. During this time period at the prevailing tunnel speed, the vortex was convected by 2 chord lengths downstream and was assumed having passed the probe volume location. Time dependent data acquisition was started each time after a defined blade position reference signal arrived, which had a fixed phase to the periodic flow field. Data acquisition was performed over many rotor revolutions to obtain a sufficiently high number of individual velocity data. The acquired time dependent velocity data for the total measurement window was subdivided into a chosen number of subintervals (classes) and the velocity data were averaged in each class. For a typical measurement window of 45° azimuth and angular resolution of 0.5° the number of classes was 90. The temporal position of the time subinterval was consequently converted into the corresponding spatial position using an estimate of the convection velocity of the vortex (e.g. the mean velocity vector of the complete measured flow field). Finally, the complete velocity field of the considered vortex section was established in rotor fixed Z, X-coordinates.

Blade Deflection Measurements

Aeroelastic blade deflections, especially torsional and flapwise deflections represent important parameters affecting BVI noise and vibrations. Three different techniques were applied to obtain the required information. The first one was the conventional *strain gauge technique*, which made use of the 32 strain gauges installed in the pressure instrumented blade, to calculate the torsional, flapwise, and in-plane deflections along the blade span. This technique, provides results for all azimuth angles, but the deflections are generally coupled to a certain degree. The accuracy may be improved by adjustments based on direct blade tip deflection measurement results,

e.g. from the TART and/or the PGM methods (see below).

The second technique, which provided flapwise and torsional deflections along the blade span at selected azimuth angles, was the so called *Projected Grid Method (PGM)* developed for application by DNW. The method is based on the fact that a grid, which is projected on the surface of a structure from a certain direction and viewed (or recorded) from a different direction, changes its image when the structure is deformed or displaced. By comparing the image of the non-deformed blade with the one of the deformed blade, the relative deformation and displacement of the structure can be determined. For HART, the grid was projected in the darkened test section perpendicular to the leading edge of the dull white painted blades. This resulted in a parallel shift of the grid pattern (with change of the spacing) in case of a vertical blade displacement and in a skewed shift of the grid lines in case of blade torsion. The projection was made from a specially constructed bench installed underneath the rotor on the test section floor with the center of rotation vertically aligned with the rotor center (Fig. 8). The bench was equipped with the grid projector and a high resolving CCD camera and could be turned over the range of 360°. Once adjusted at a pre-selected fixed position, the arrangement allowed to record the grid pattern at any desired blade azimuth position by adequately triggering the video camera. Reference measurements were made at zero thrust hover condition with correctly set rotor shaft angle.

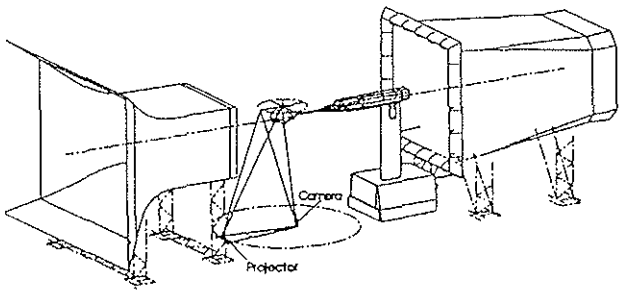

Fig. 8 Set-up for the Projected Grid Method (PGM).

The third method called *Target Attitude in Real Time (TART)* method was provided by ONERA to measure the blade tip deflections. The system consisted of a CCD camera and a PC. The TART system recorded the image of two retroflecting circular tapes, stuck at the blade tip and illuminated by means of a stroboscope. The barycenters of the two spots were transmitted via a special interface to a PC, which displayed the angle of incidence as well as the position of the blade tip in the rotor fixed coordinate system in real time.

Test Conditions and Test Sequence

The test matrix covered a range of simulated flight conditions of low and moderate speed descent with flight path angles ranging from 0° to 12° descent. Emphasis was put on descent conditions known to generate intensive BVI impulsive noise, but also a small number of level flight, climb, and hover conditions were included. The advance ratio was varied between μ=0.114 and 0.273 with different shaft angle sweeps between α_s=-4.5° and 11.3°. Nominal thrust coefficient was C_T=0.0044. The nominal rotor operating speed maintained constant throughout the test was 1040 rpm (corresponding to a nominal hover tip Mach number M_H=0.64), giving a blade passage frequency of approximately f_{bp}=70Hz. All test runs were conducted with the rotor trimmed to zero hub moments, i.e. the tip-path-plane angle, α, was assumed perpendicular to the measured shaft angle, α_s, with positive values corresponding to backward tilt. Equivalent results for model-scale and full-scale flight testing can be expected when the non-dimensional rotor parameters μ, α', C_T and M_H are trimmed to identical values for model- and full-scale. α' is the corrected tip-path-plane angle which takes into account the effect of the finite open-jet potential core (Ref. 23).

Aerodynamic blade pressure and acoustic measurements were conducted for the full matrix of test conditions without HHC (called baseline cases BL) and with HHC activated. For a typical BVI condition (6.5° descent at μ=0.15, α_s=5.3°) denoted nominal BVI test condition, systematic HHC variations were conducted including 3P, 4P, 5P modes and phase variations. Conditions with special HHC schedules for which BVI noise or vibrations were found minimized, have been termed Minimum Noise (MN) or Minimum Vibration (MV) HHC cases. Some operational variations at different μ and α_s were focused on this (3P) HHC mode with phase angle for MN or for a small interval near this phase angle to study the effectiveness of a fixed HHC schedule to reduce BVI noise at different flight conditions. The LLS, LDV, PGM, and TART measurements were exclusively conducted for five conditions: the nominal BVI BL case, the MN and MV HHC cases, and two baseline cases at μ=0.15, α_s=3.8° and 6.8°.

The aeroacoustic measurements were followed by the LLS flow visualization tests to quantitatively determine vortex trajectory segments and blade-vortex miss distances. In the following the LDV measurements were conducted to determine vortex core size, vortex circulation strength, and local blade-vortex miss distance. Finally, complementary to the strain gauge measurements, blade deflections (torsion and flapping) were measured by PGM and blade tip deflections (torsional, in-plane, flapwise) by TART.

Prior to starting the measurement program, reflection tests employing small explosive charges placed in the rotor plane, verified both the anechoicness of the test environment and the insignificance of acoustic shielding or diffraction from fuselage or model sting for the BVI noise measurements. Wind tunnel background noise measurements at different wind speeds confirmed excellent signal-to-noise ratios of more than 25dB in the mid-frequency range dominated by BVI noise. After 23 days of wind tunnel occupancy time, the tests were completed in June 1994. Initial test results have been reported in Ref. 24.

ACOUSTIC TEST RESULTS

Quality Considerations

Steadiness of test conditions and repeatability and consistency of the aeroacoustic measurement results were verified by repeat tests. In Fig. 9 sound pressure and blade surface pressure histories (average and standard deviation from 12 repeats) for nominally identical test conditions (μ=0.15, α_s=5.3°) are shown, illustrating the high degree of data quality obtained for this typical BVI baseline case. The impulsive acoustic waveform in part (a) was generated by the blade pressure fluctuations (part (b)) in the first quadrant (15° < ψ < 75°); the pressure fluctuations in the fourth quadrant (280° < ψ < 330°) indicate significant retreating side BVI as well.

Noise Directivity and Intensity

In Fig. 10 (a-d) is shown how mid-frequency noise (L-MF) directivity was changed by different modes and phases of HHC at fixed amplitude θ_c. All cases were taken for the same simulated descent flight at flight path angle θ_{fp}=6.5°, μ=0.15, α_s=5.3°, α'=4.2°, termed the nominal BVI condition. To emphasize the more important radiation lobes, only the higher level contour lines have been plotted. Control phase angles ϕ (based on measured values) and related azimuth control angles ψ_c, which define the azimuth where HHC pitch is a minimum, are noted on each plot. The baseline (BL) directivity is shown in part (d) of Fig. 10. A significant influence of phase on BVI noise directivity and intensity is seen in part (a) for 3P HHC at θ_c=-0.85°. The contours indicate a substantial modification of the BVI occurrences with elimination of certain interactions or commencement of others. Retreating side BVI is decreased for a phase angle range of 38° ≤ ψ_c < 98°. Most effective reduction of the advancing side BVI noise directivity lobe (from all HHC variations tested) is seen for ψ_c=38° (ϕ=296°). This minimum noise condition was denoted MN case. At other phase angles the noise intensities are increased. This is especially the case for ψ_c=119° (ϕ=117°). At this operational condition the vibration level (explained later) was found to be minimized for 3P HHC. This minimum vibration condition was termed MV case. Similar observations can be made for 4P and 5P HHC in part (b) and part (c), respectively. Retreating side BVI noise is seen reduced for many phase angles, while advancing side noise is increased for some phases and reduced for some others, however, not as effectively as for 3P HHC.

More specifically, the influence of HHC variations on noise and vibration levels is shown in Fig. 11(a-r) for the

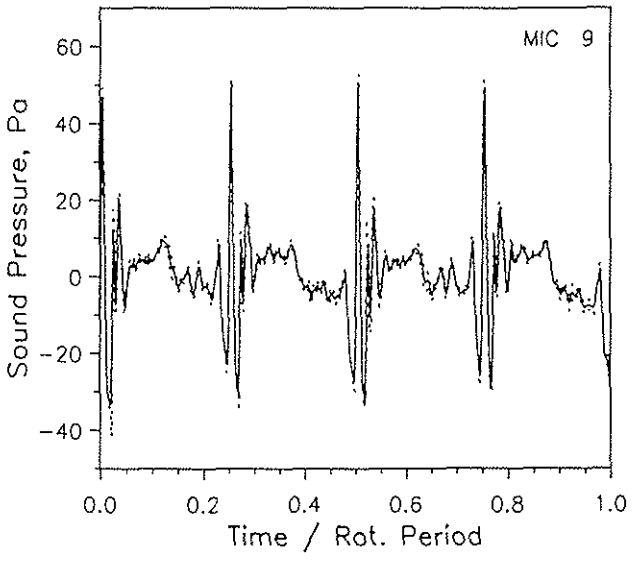

(a) Sound pressure histories

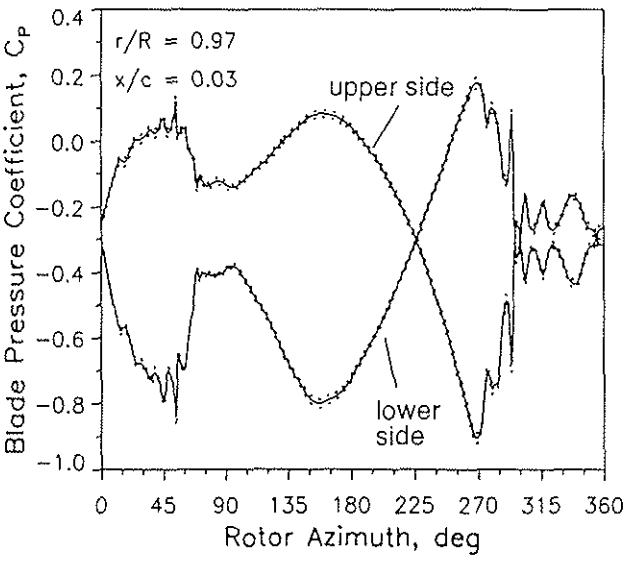

(b) Blade surface pressure histories

Fig. 9 Typical acoustic and blade pressure histories (avg ± σ) of 12 repeat cases for θ_{fp}=6.5° descent at μ=0.15, α_s=5.3°, α'=4.2°.

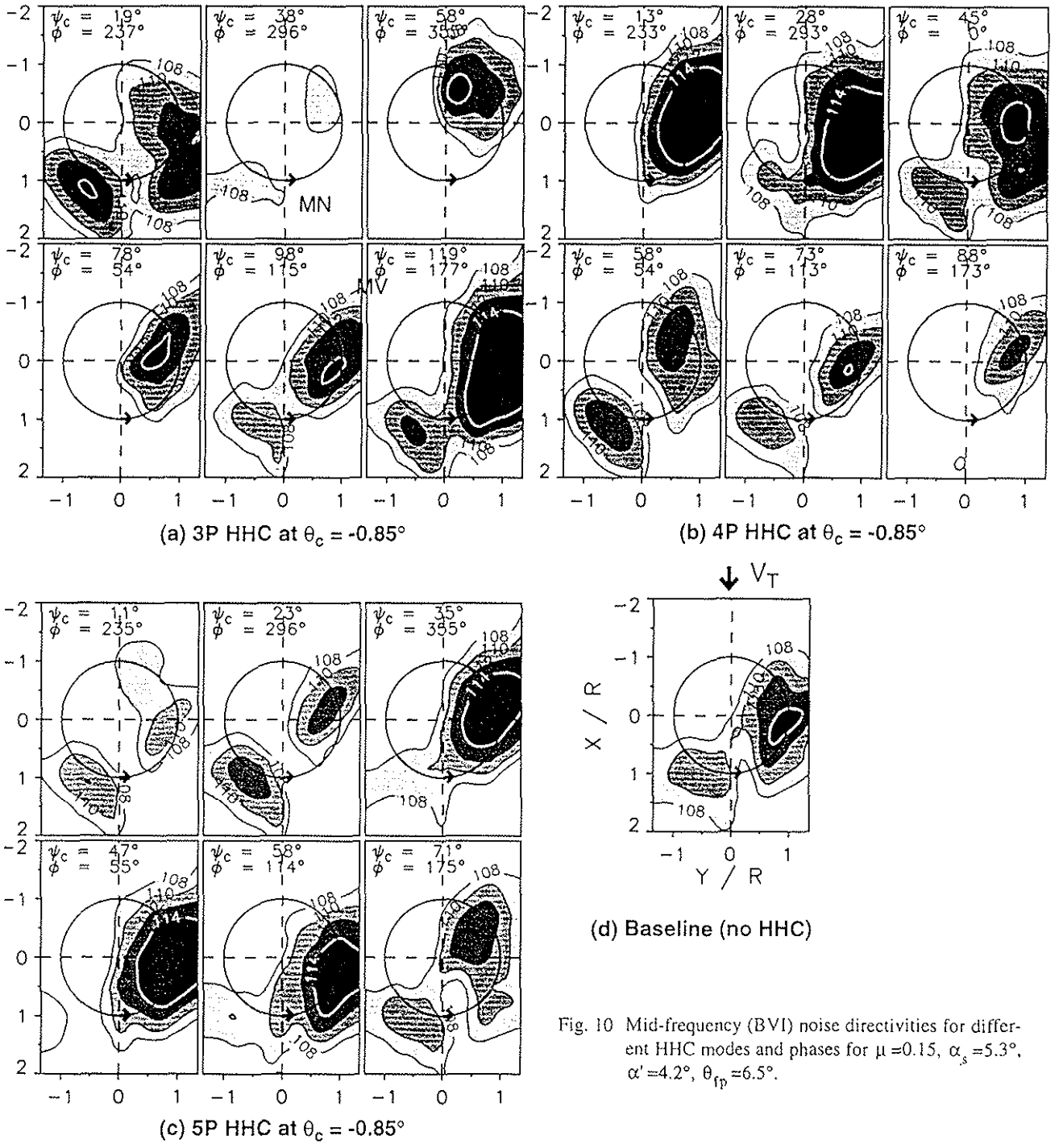

Fig. 10 Mid-frequency (BVI) noise directivities for different HHC modes and phases for μ =0.15, α_s =5.3°, α' =4.2°, θ_{fp} =6.5°.

same rotor condition as for Fig. 10. Different noise evaluation measures (mid-frequency, low-frequency) and a vibration quality criterion are plotted for different HHC modes (3P, 4P, 5P) and fixed HHC amplitude (θ_c =-0.85°) versus azimuth control angle ψ_c. The data for the baseline case is indicated by a dashed line on each plot. Advancing and retreating side maximum L-MF values (parts (a-c) and (d-f)) have been determined separately from the acoustic measurement plane underneath the first to the third quadrant and underneath the fourth quadrant, respectively. Effective noise reductions but also increased noise levels are identified for all three control modes; most effective reduction of the advancing side maximum level (order of 6dB; first minimum of the curve) was obtained for 3P control at ψ_c =38° with a secondary minimum at ψ_c =88°, as shown in part (a). For 4P and 5P HHC smaller noise benefit was measured at related control angle ranges near ψ_c =88° for 4P and between $0 \le \psi_c \le 23$ ° for 5P. Significant noise reductions and similar trends are seen for retreating side BVI as illustrated in parts (d-f). Maximum reductions (approx. 4.5dB) were measured for 3P at ψ_c =48° and 4P at ψ_c =88°. 5P control was much less effective. At 3P HHC the phase angles for maximum noise reduction of the advancing and retreating side BVI noise sources are slightly different ($\Delta\psi_c$ =10°); this implies that both sources cannot be simultaneously

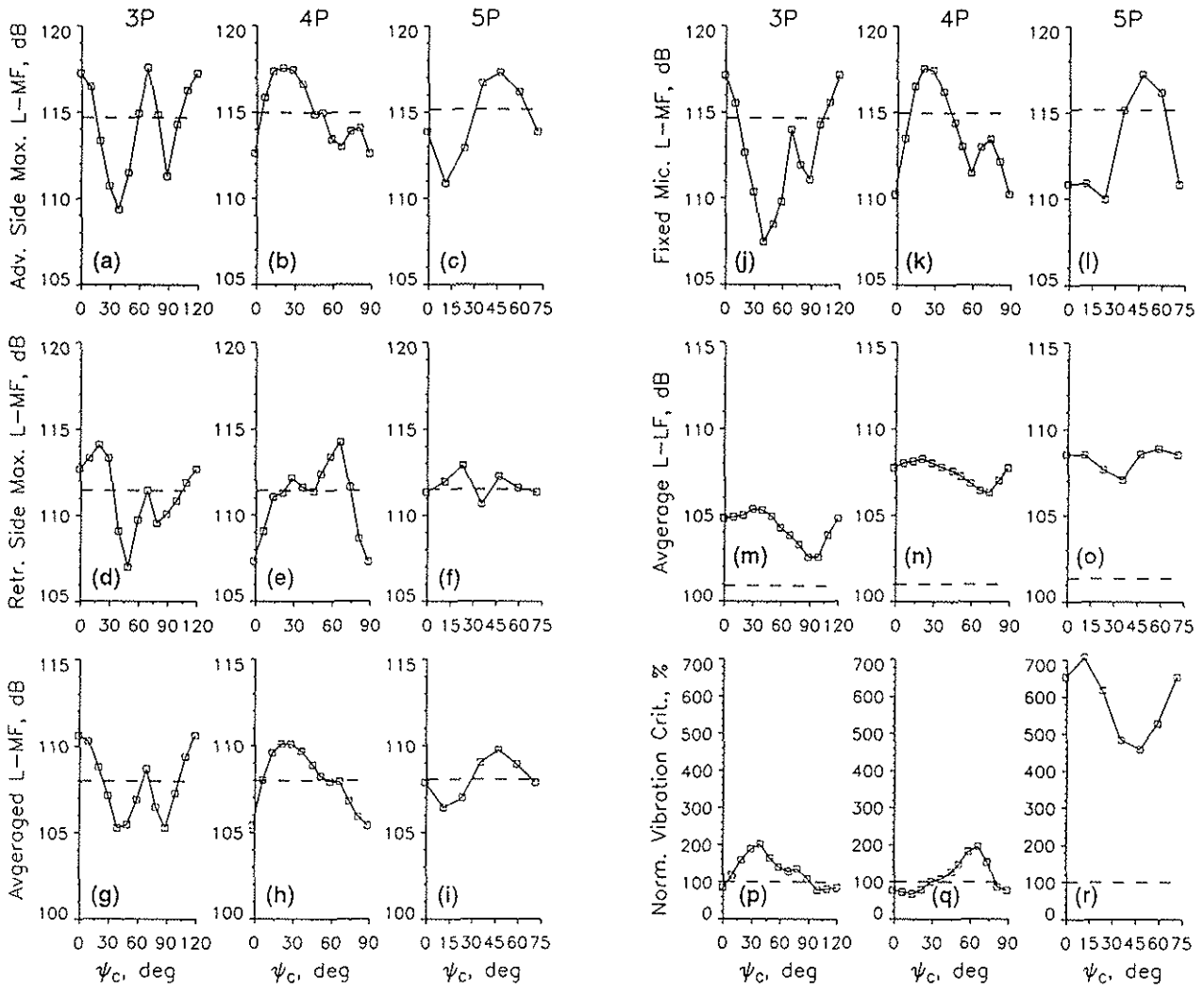

Fig. 11 Noise and vibration levels versus azimuth control angle for different HHC modes for the typical BVI condition of Fig. 10 baseline w.o. HHC: - - - - .

controlled in an optimal way by HHC for this considered test case.

Spatially averaged BVI noise levels (parts (g-i)) show somewhat less noise reductions (order 3dB) for 3P and 4P HHC, while 5P again is rather ineffective. Parts (j-l) show L-MF values for a fixed microphone location (mic 9 at X/R=0.5), where maximum advancing side BVI noise was measured for the baseline case. Similar trends as for the advancing side max. L-MF (parts (a-c)) are observed, however, larger noise reductions are seen for each control mode (order 5 - 7dB), probably an additional effect of maximum BVI noise directivity changes. Spatially averaged low-frequency noise levels (L-LF) are presented in parts (m-o). Compared with the baseline case, the L-LF values are substantially increased due to low frequency loading noise generated by the HHC pitch motion. The highest levels were observed at 4P and 5P control (order 7dB), the lowest at 3P (order 4dB). However, it is important to note that on a subjective A-weighted dB scale, the low frequency noise is not of concern compared to the mid-frequency BVI noise.

The vibration quality criteria calculated from the 4P components of the rotor balance forces and moments and normalized to the baseline case vibrations are shown in parts (p-r) of Fig. 11. Inertial forces due to the accelerating masses of the swash plate, blade root hardware, actuator pistons, and other control hardware used to produce the HHC pitch motion have been compensated for by proper calibration. Minimum vibration was identified for 3P and ψ_c=119° (ϕ=177°) and termed minimum vibration (MV) case. Unfortunately, the intensity of BVI noise radiation was distinctly increased (by 2.5dB) for this MV case as compared to the BL case (see Figs. 10(a) and (d)). In general, increased vibration levels were measured at reduced BVI noise control settings and lower levels when L-MF was seen increased. This is quite consistent with findings in Refs. (13-15). However, for 3P and 4P pitch control a number of azimuth control angles (ψ_c ranges) were found for simultaneous noise and vibration reduction (see parts (a, p) and (b, q)). Also, the absolute vibration levels do not

appear prohibitive in the low speed descent flight regime, where application of HHC for noise reduction would be most effective, except probably for 5P HHC. For 5P control mode extraordinary increase in vibration level (factor of 5 to 6 above baseline case) was determined, a result of a strong X-force component measured by the rotor balance. This increase of the axial force can be attributed to an excitation of the blade's second lead-lag mode, which has a natural frequency close to 5P and only a small structural damping.

The maximum noise benefit of about 6dB is in agreement with previous findings for nominally the same rotor. Also, HHC control angles ψ_c for minimum noise are similar to those of Ref. (15), however slightly shifted by a few degrees to lower ψ_c values. But in Ref. 15, largest noise reductions were obtained for a different HHC mode and amplitude (4P and θ_c=-1.2°). This probably was caused by small differences in blade dynamic properties (slightly more soft in torsion) of the instrumented blades used in this test and the non-instrumented ones used previously.

Operational Variations

The effectiveness of a fixed HHC schedule (e.g. that for MN) to reduce BVI noise at different flight conditions was investigated by variation of θ_{fp}, μ, and C_T while maintaining 3P HHC at θ_c=-0.85° and ψ_c=38° (ϕ=296°) constant. Noise reduction benefit was seen for rotor conditions close to the nominal BVI condition (μ=0.15, θ_{fp}=6.5°), while at other flight conditions (e.g. μ=0.15, θ_{fp}=9.0°) increased noise levels were measured; however, when changing the HHC phase (e.g. by $\Delta\psi_c$=60°, corresponding to $\Delta\phi$=180°) significant noise reductions were obtained. This is in agreement with the results in Ref. 15 and suggests the application of "closed loop" HHC for optimum noise reduction at different flight conditions.

Noise Characteristics of Selected Test Cases

Among all HART test cases, three special configurations (termed BL, MN, MV) have been selected for analysis and illustration of the experimental results presented in this paper. Where appropriate for interpretation, a few additional test cases have been included in the analysis. The noise characteristics of these three distinctive test cases are shown in Fig. 12. The baseline case L-MF directivity plot in part (a) shows two distinct noise radiation lobes generated by advancing side and retreating side BVI occurrences, respectively, which is consistent with previous studies (e.g. Refs. 14). The use of MN HHC settings (3P, ψ_c=38°) significantly changed the directivity levels. Adv. side peak levels are seen reduced by approx. 6dB, while the retr. side levels are reduced by 2dB. For MV control settings (3P, ψ_c=119°), the adv. side BVI noise levels are increased by more than 2dB and those of retr. side by 1dB. In addition, for the MN case the noise radiation is directed more forward indicating that the BVI occurrences have moved upstream toward 90° azimuth as is confirmed in Fig. 15(a),(b) and Fig. 16.

Averaged sound pressure histories (30 avgs) are shown in part (b) for the noisiest locations of the L-MF contours of part (a). For the BL case, the typical positive pressure spikes of adv. side BVI are seen, which are of opposite polarity for retr. side BVI. The pressure histories for MN and MV HHC control settings feature increased low frequency noise primarily at the blade passage frequency. The impulsive content of the signatures for MN is distinctly reduced, while increased spikes on the retr. side and multiple BVI signatures on the adv. side are seen for the MV case. The low frequency noise increase is due to the higher harmonic blade loading and may be a matter of concern for application of HHC. But, it should be noted that the measurement plane is in the acoustic near field for low-frequency noise but in the farfield for BVI noise sources. This may lead to overestimate the importance of the low-frequency contribution, and with regard to subjective dBA or PNL measures, the observed low-frequency noise increases contribute very little. All these changes of the noise characteristics resultant from the different HHC inputs, are caused by strong modification of the unsteady blade pressure (loading) distributions in the first and fourth quadrant of the rotor plane (discussed in the next chapter).

AERODYNAMIC RESULTS

Blade Airload Characteristics

An important feature to allow a better insight into the BVI phenomenon and into the effects of HHC on the important aeroacoustic characteristics constitutes the measurement of the unsteady blade surface pressures. A sample of a typical upper and lower surface pressure history was shown in Fig. 9(b). Sectional blade airloads (normal forces C_N) were calculated by integration of the measured blade pressures at each of the three densely instrumented radial sections. C_N is defined as the aerodynamic force per unit area normal to the blade chord, normalized to the local chord (here constant) and the relative dynamic pressure. With local Mach number M the nondimensional normal force $C_N M^2$ was calculated, a quantity which is more truly representing the actual aerodynamic forces. In the multi-part Fig. 13, $C_N M^2$ histories at section r/R= 0.87 for the nominal (6.5° descent) BVI case are shown, illustrating the influence of HHC mode and phase variations (parts a-c) on the sectional blade airload (or lift) in comparison to the baseline case without HHC (part d). The BL case shows distinct loading fluctuations due to BVI in the first and fourth quadrant of the rotor plane between $15° \le \psi \le 75°$ and $280° \le \psi \le 330°$.

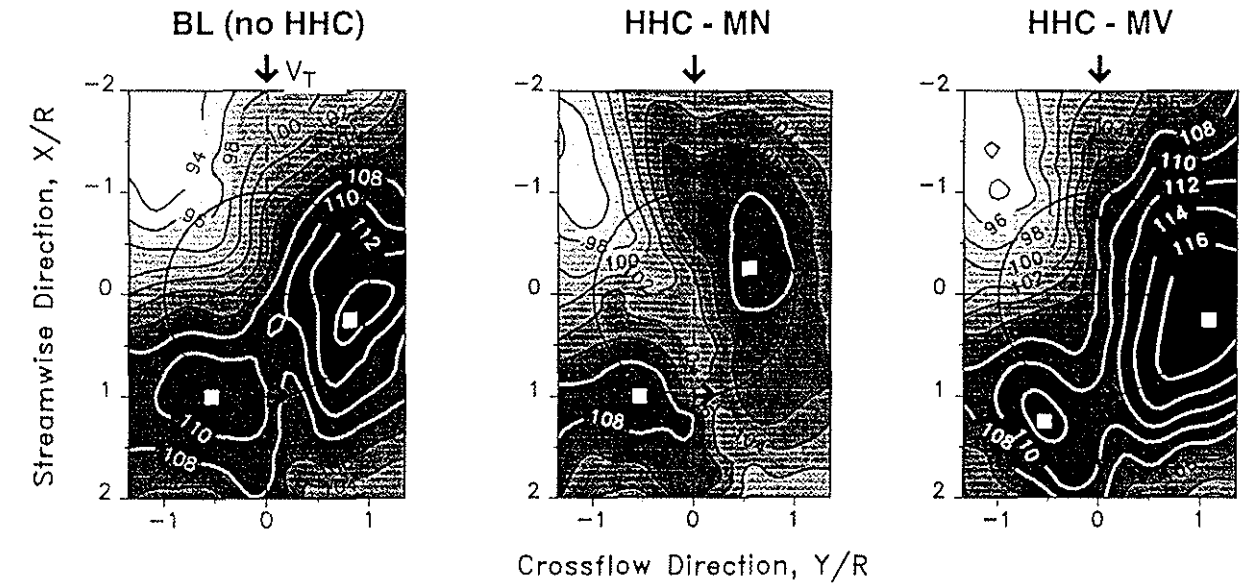

(a) L-MF (BVI) noise directivities (top views on measurement plane)

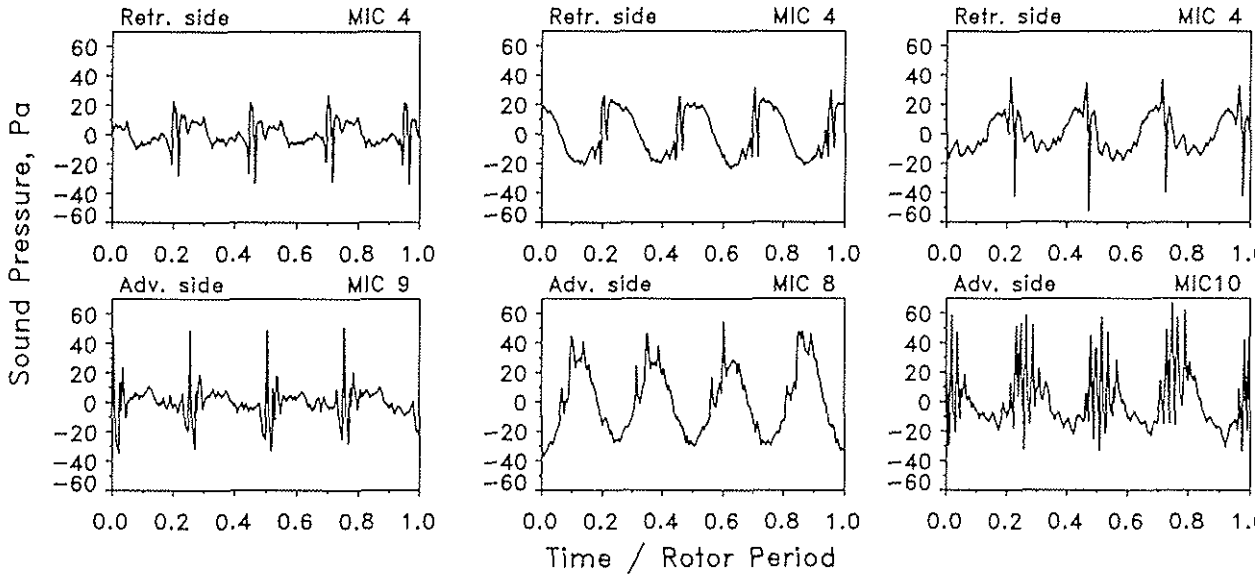

(b) Sound pressure histories at noisiest locations (□)

Fig. 12 BVI noise directivity and acoustic signatures for BL, MN, and MV HHC cases for typical BVI condition at $\mu=0.15$ $\alpha_s=5.3°$, $\alpha'=4.2°$, $\theta_{fp}=6.5°$.

As expected from application of higher harmonic blade pitch control, strong changes of the measured sectional blade airloads were observed when, at fixed HHC mode and amplitude, the phase was systematically shifted by increments of $\Delta\phi=30°$. The results for 3P HHC are shown in part (a), where only every second phase variation is displayed ($\Delta\phi \approx 60°$). Quite obvious are low frequency (3P) oscillations generated by the 3P HHC schedule applied. But more important for BVI noise reduction is the fact that a distinct smoothing of the BVI induced loading fluctuations between $30° \le \psi \le 65°$ is seen for a control phase angle that exactly corresponds to the HHC-MN setting of $\psi_c=38°$ ($\phi=296°$). Some reduction of impulsive content of the loading waveform is also seen at control angle $\psi_c=58°$ in the azimuth range $270° < \psi < 330°$ indicating a reduction of retreating side BVI (see Fig. 11(d)). On the other hand, increased loading fluctuations are visible at the acoustically sensitive azimuth ranges ($30° < \psi < 70°$ and $300° < \psi < 330°$) for a number of HHC phase settings including the one corresponding to the HHC-MV setting of $\psi_c=119°$ ($\phi=177°$). The time derivatives of these force fluctuations are responsible for the increased noise levels and the modified noise directivity patterns observed for the corresponding conditions in Fig. 10(a). Similar observations can be made for 4P and 5P HHC modes of Fig. 13(b) and (c). In part (b) impulsive fluctuations on the adv. side are minimized for azimuth control angle $\psi_c=88°$ which corresponds well to the low-

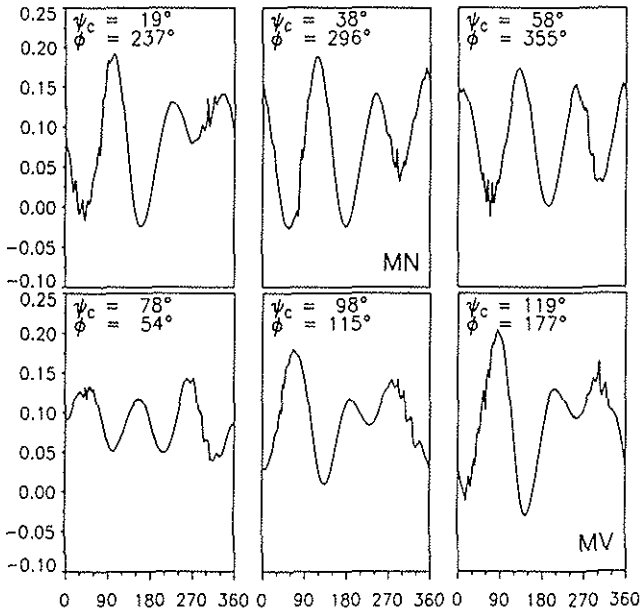

(a) 3P HHC at θ_c = -0.85°

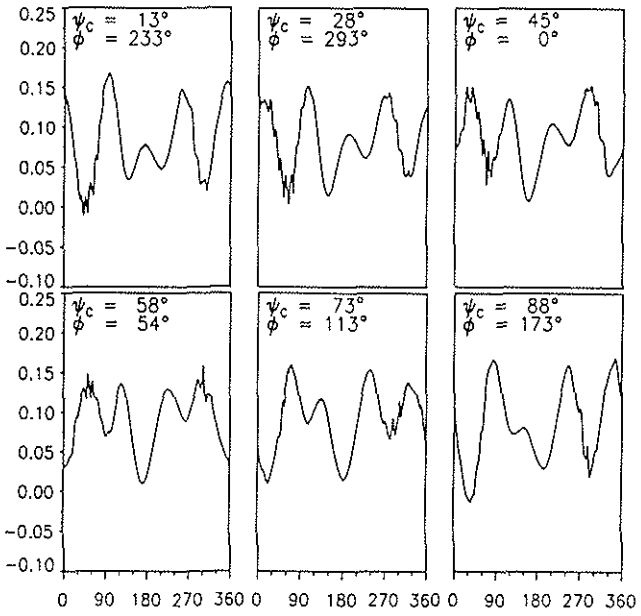

(b) 4P HHC at θ_c = -0.85°

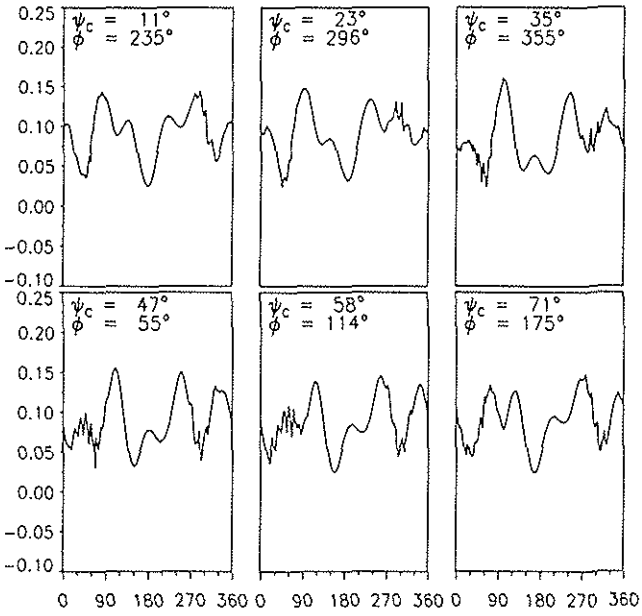

(c) 5P HHC at θ_c = -0.85°

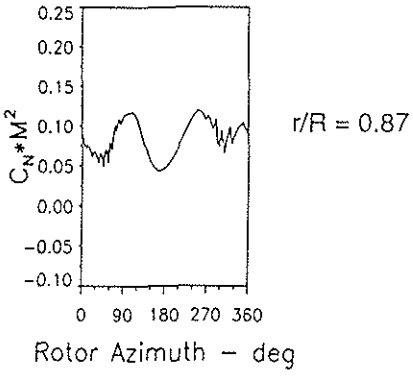

(d) Baseline (no HHC)

Fig. 13 Sectional blade airload histories for different HHC modes and phases for rotor conditions as for Fig. 10.

est adv. side BVI noise level measured for this control phase angle (see Fig. 11(b)). This is also true for the 5P mode at control angle ψ_c=11° (compare Fig. 13(c) and Fig. 11(c)).

The blade airload results also contribute to a better insight into the rotor wake behaviour, the tip vortex strengths, and the blade-vortex interaction geometry. In Fig. 14 unfiltered $C_N M^2$ contours have been plotted for the three distinctive test conditions BL, HHC-MN, HHC-MV which illustrate the normal force (or lift) distribution on the outboard part of the rotor plane. The white patches indicate high positive lift, the black areas negative lift. From close inspection of Fig. 13(a) and Fig. 14 the highly important role of blade airloads and of the change of airloads with HHC becomes clear. In Fig. 13(a) at MN control input (ψ_c=38°) the blade airload as compared to the baseline case in part (d) is seen largely reduced (even showing negative values) in the first quadrant at the azimuth range of strong advancing side BVI ($30° < \psi < 65°$) and strongly increased in the second quadrant where the interacting vortices have been generated ($120° \le \psi \le 150°$). Similar observations are valid for the retreating side, where BVI occurs near ψ=300° and the related vortices have been generated near ψ=240°. The conclusions for this minimum noise control setting are: due to the increased airload (bound circulation) in the second quadrant (1) the circulation of the trailing tip vortex, the vortex strength, was enlarged and (2) the induced velocity field (downwash) in the blade wake was highly increased

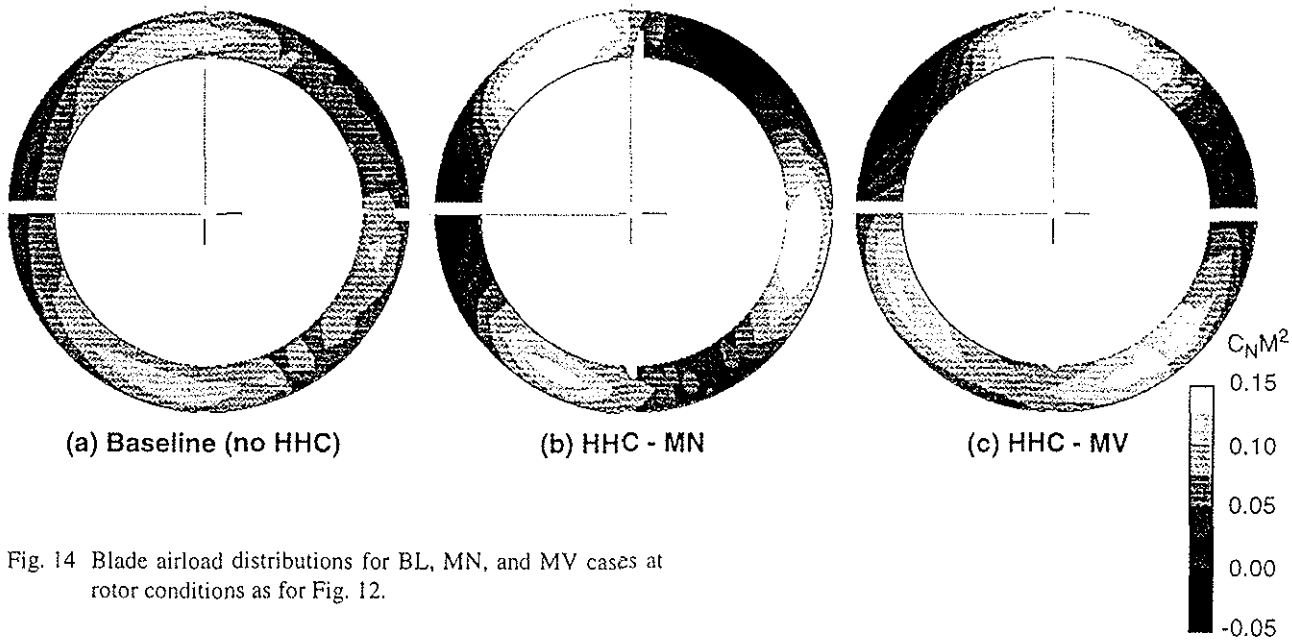

Fig. 14 Blade airload distributions for BL, MN, and MV cases at rotor conditions as for Fig. 12.

with the effect that the interacting tip vortex segment, emitted in the second quadrant and convected downstream to the BVI location, was moved downwards according to the additional downwash generated (compare parts (a) and (b) of Fig. 14). This resultant wake behaviour constitutes the dominant effect of HHC on the BVI geometry and especially on the blade-vortex miss distance and was verified by the results of the non-intrusive flow and blade deflection measurements presented in the following sections.

At MV control input (ψ_c=119°) nearly the opposite trends can be observed in Fig. 13(a) and by comparing Figs. 14(a) and (c). Sectional airloads are seen largely increased in the first quadrant (BVI occurrences) and decreased to negative lift on the blade tip region in the second quadrant (vortex emission). Due to the induced upwash, the emitted tip vortex segments are pushed upwards above the rotor plane thereby significantly changing the interaction geometry and with that the miss distance (see Fig. 18(c)). This effect and the increased blade loading in the first quadrant explain the significant increase in BVI noise measured for the low vibration case. Furthermore, it appears that deloading the blade near BVI encounters would help decreasing impulsive noise intensity, but this is certainly not the prime parameter for noise reduction via HHC.

By interpreting the C_NM^2 distribution in Fig. 14(c), the phenomenon of a double vortex system near the blade tip discovered during the LLS measurements for MV HHC settings (see below) can also be explained. The negative lift measured on the blade tip region in the second quadrant is an indicator for a spanwise bound circulation distribution with strong radial gradients at the tip and also somewhat inboard where blade loading switches sign. Separate vortex roll-up (clockwise inboard and counter-clockwise at the tip) is likely to occur near such designated radial locations.

In-plane BVI Locations

Very useful for wake code validation including multicyclic pitch control is information on the in-plane BVI geometry determined from the measured pressures near the leading edge (x/c=0.03). Making use of the valleys and peaks of the differential surface pressure histories (Ref. 25) at each advancing and retreating side, respectively, the actual BVI locations in the rotor plane were identified. The results for the considered cases BL, MN, and MV and three additional baseline conditions (μ=0.15, α_s=-0.7°, 3.8°, 6.8°) are presented in Fig. 15(a-f), where symbols are plotted on the ΔC_PM^2 contours which inherently contain this information.

For the baseline case in part (a) quite a number of interactions are seen in the first and fourth quadrant with acoustically important (parallel) BVI's at about ψ=46° and 55° and further at ψ=305° and 315°, respectively. In the downstream region near ψ=0°, the wake appears distorted from interactions with the rotor hub. For the MN case (part (b)) the BVI locations on the advancing side are seen shifted upstream beyond ψ=60°; the dominant parallel interactions apparently are completely avoided. The retreating side BVI locations have moved upstream as well with only one remaining parallel interaction near ψ=305°. For the MV case (part (c)) important BVI locations are seen between ψ=30° and 60° and at similar locations as for the BL case on the retreating side. For the level flight baseline case (part (d)), a reduced number of BVI locations are grouped around ψ=90° and 270°, while for the two descent cases at θ_{fp}=5° (part (e)) and 8° (part (f)) the BVI

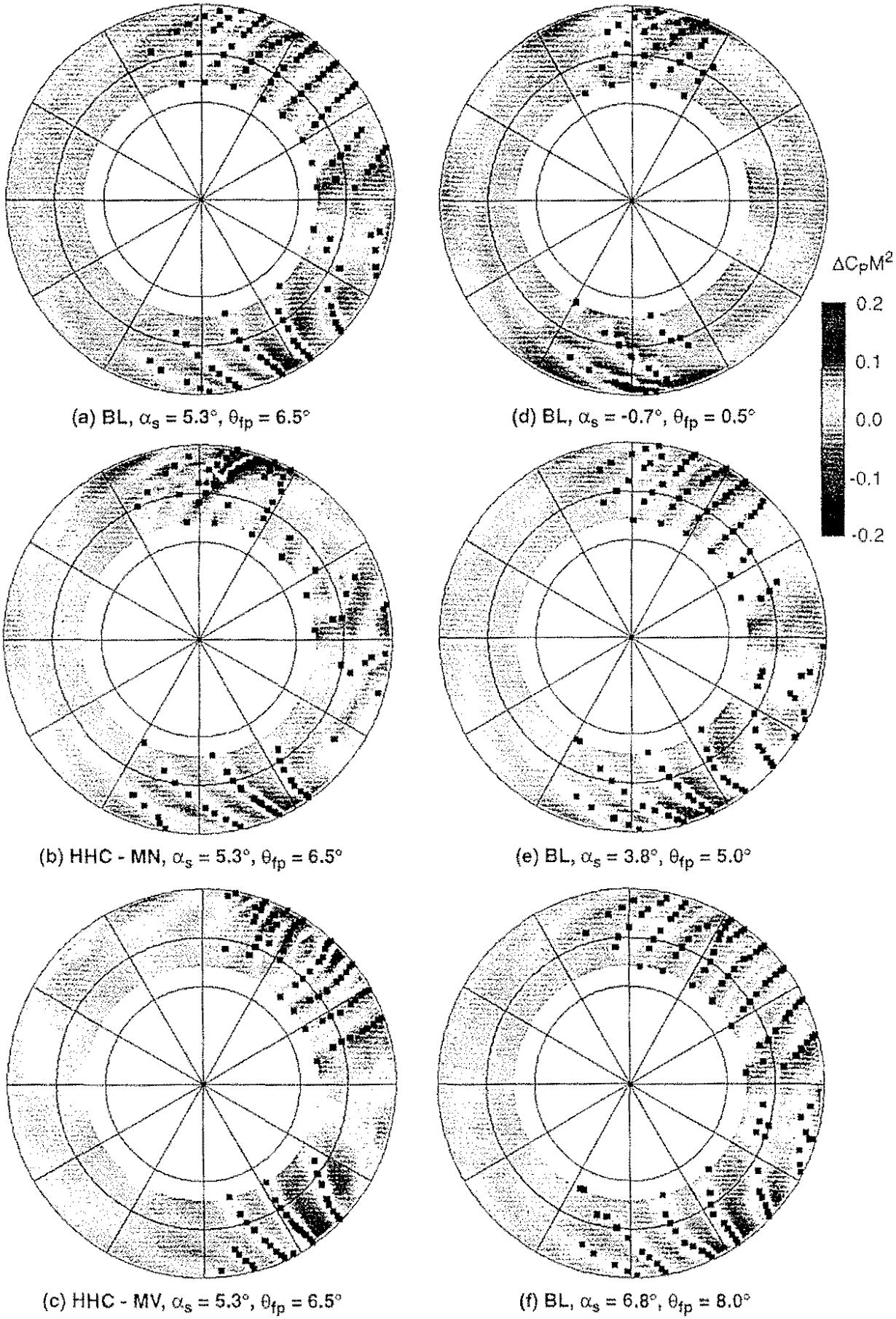

Fig. 15 Experimental BVI locations (top views) for different descent conditions at $\mu = 0.15$.

locations move downstream with increasing backward tilt of the tip-path-plane indicating parallel BVI's similar to the 6.5° descent baseline case. Correlation of some of these experimental results with HART pre-test and post-test predictions are presented in Refs. (26, 27).

A comprehensive and illustrative representation of both important aerodynamic and acoustic results is provided in Fig. 16(a-c) showing perspective views of high pass filtered (> 6P) $\Delta C_p M^2$ distributions in the rotor plane (measured near the leading edge at x/c=0.03) as well as the L-MF contours of the radiated noise field below the rotor. The BL case (part (a)) nicely illustrates strong blade pressure fluctuations in the first and fourth quadrant responsible for advancing and retreating side BVI noise radiation shown below. These strong pressure fluctuations in the critical azimuth range between 40° and 60° have been significantly smoothed for the MN pitch schedule (part (b)) and BVI noise radiation is distinctly reduced, while for the MV case largely increased pressure fluctuations in the sensitive azimuth range are seen with correspondingly increased BVI noise radiation (note that the upstream portside, dark areas are of lower L-MF level and should be disregarded).

FLOW VISUALIZATION RESULTS

Change of Vortex Structure

Immediate illustrative results of the LLS flow visualization test are video recording images of cross-sections through any desired tip vortex which is properly seeded with oil smoke and illuminated by the laser light sheet.

From these recordings static pictures may be selected at that instant in time when a blade passes by or encounters the vortex. Samples for the nominal BVI BL case and the MN and MV HHC cases are illustrated in Fig. 17. The interacting vortex of the baseline case observed near azimuth ψ=50° is seen displaced below the blade and more diffused for the MN case. Quite surprising and not seen before was the detection of a double vortex system for the MV control schedule comprising a clockwise vortex near the rotor plane and a counter-clockwise vortex above the first one. Both being emitted in the plane of rotation have changed position by mutual induction.

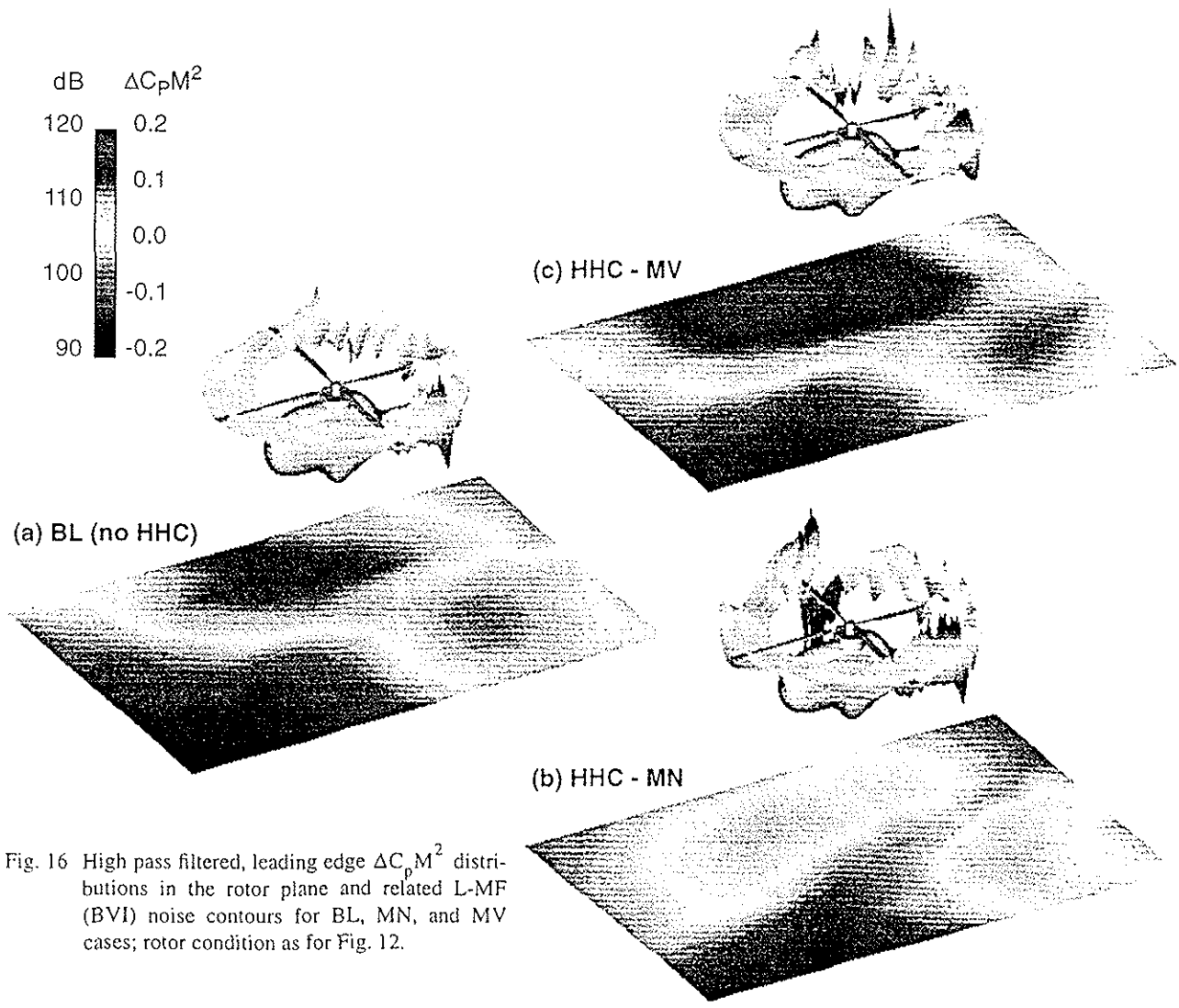

Fig. 16 High pass filtered, leading edge $\Delta C_p M^2$ distributions in the rotor plane and related L-MF (BVI) noise contours for BL, MN, and MV cases; rotor condition as for Fig. 12.

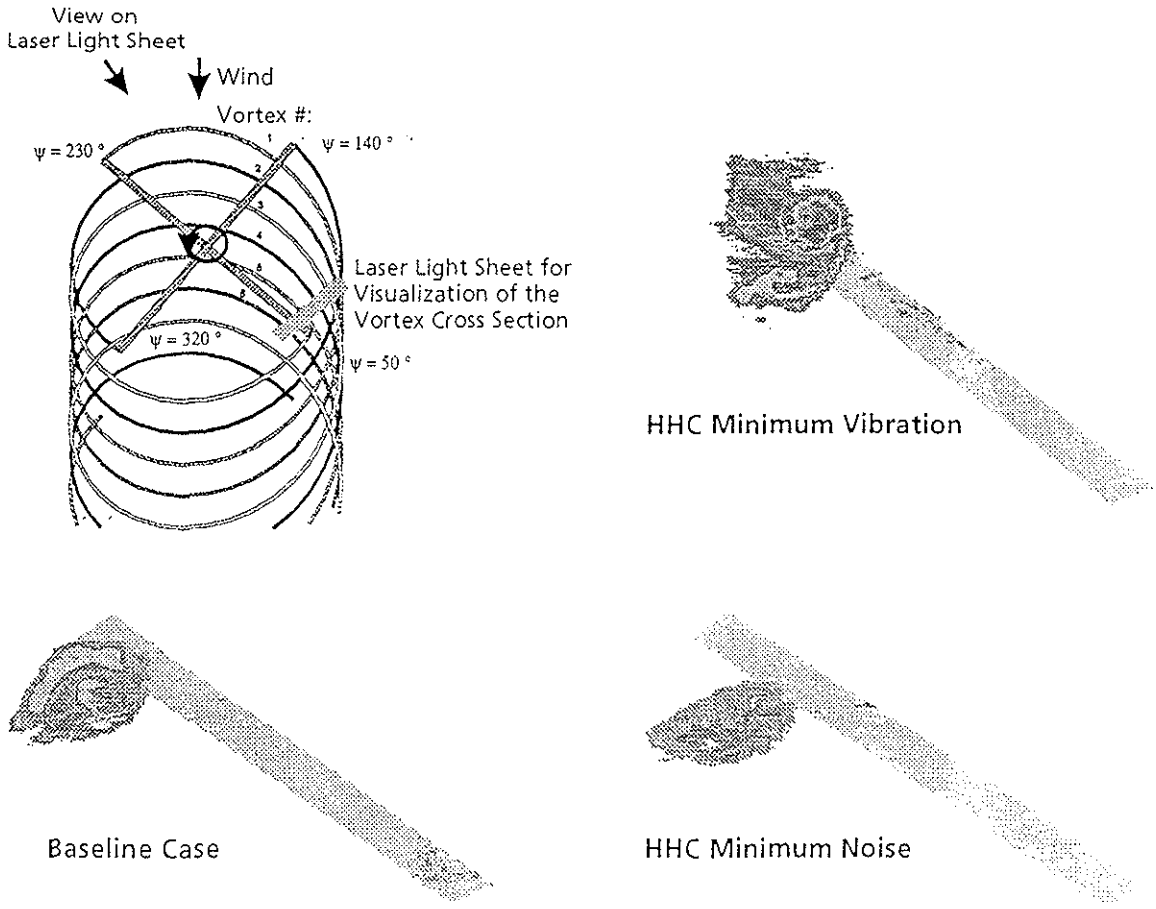

Fig. 17 Visualization of the tip vortex structure by LLS for BL, MN, and MV cases of a blade-vortex interaction near ψ =50°; rotor condition as for Fig. 12.

Tip Vortex Geometry and B/V Miss Distance

Beside these more qualitative results also quantitative results have been accomplished with the LLS technique. Vortex geometry segments of two tip vortices (most significant for BVI) on each the advancing and retreating side were obtained from measuring the vortex core centers in space (in the rotor fixed coordinate system with origin at the hub) of at least four discrete sections along the vortex of interest. The data were measured for particular "frozen" blade azimuth positions of ψ =35° and ψ =295°, respectively. In addition, the blade position was measured for these azimuth locations. The results for the BL case, the MN and MV HHC cases are plotted in Fig. 18, which illustrates both the top views and the side views of the wake geometry segments with parts (a)-(c) for the advancing side and parts (d)-(f) for the retreating side. In the top views, the Z-axis represents the vertical axis of the wind tunnel, X- and Y-axis define a horizontal plane in which the blade position as well as the measured tip vortex segments are plotted. In the side views (frontal to the blade as indicated by an arrow) the Z-axis represents the rotor shaft axis and the R-axis the blade span; therefore, the Z-R plane contains the rotor axis and the blade quarter-chord line. (It should be noted that in the top views the Z-axis used is not exactly the shaft axis, but is close to it because of small shaft angles α_s.) In the frontal views, the actual shape of the deformed blade is plotted, so that the "vertical" distance between the blade and the vortices provides an estimate for the "miss distance"; but it should be realized that this distance is not exactly the blade-vortex miss distance because the measurement data were acquired at fixed azimuth of 35° and not at the azimuth of interaction (near 46° and 55°). Similar remarks are valid for the retreating side LLS measurements conducted at fixed blade azimuth of 295°.

Comparisons of the BL case with the MN and MV cases of the advancing side vortex segments (top views of Fig. 18) indicate a slight upstream displacement of the vortex closest to blade for the MN case (part (b)) and a small downstream displacement and distortion for the MV case (part (c)); most interesting, however, was the identification of the double vortex system for the MV case. Com-

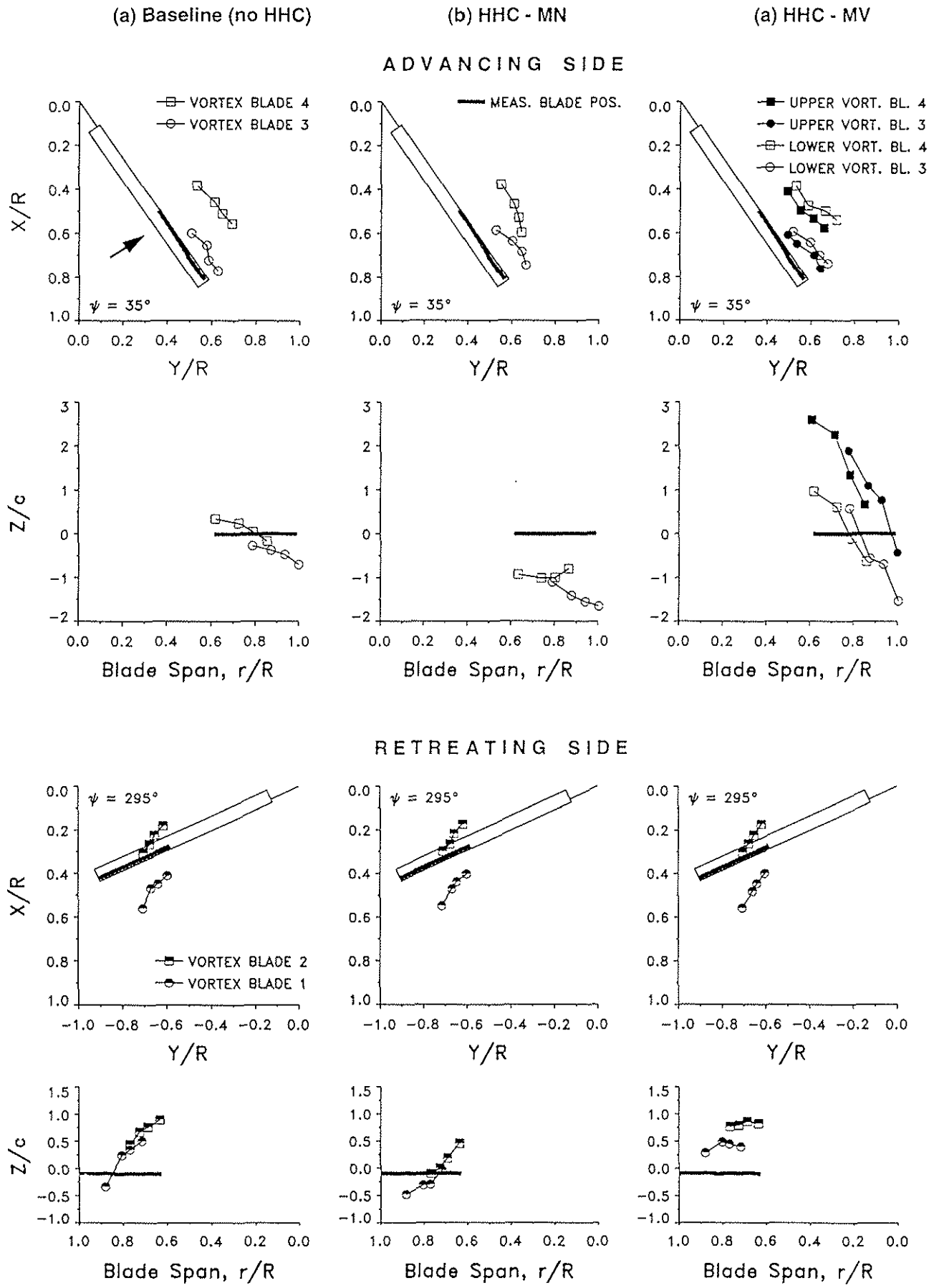

Fig. 18 Tip vortex geometry segments (top views and side views) near ψ=35° and 295° measured by LLS for BL, MN, and MV cases (side view indicating blade-vortex "miss distance"); rotor condition as for Fig. 12.

parison of the blade-vortex "miss distances" as seen in the side views yield the following observations: (1) the miss distance for the BL case is very small (0-0.5 chord,c) indicating intensive BVI noise generation, (2) at MN control the tip vortices have been convected (down) far below the blade (between 1 and 2c); this large displacement explains the observed significant noise reduction and shows that the miss distance represents the dominant parameter of noise reduction by HHC, and (3) at MV the upper and lower vortices of the double vortex system are seen cutting through the rotor plane which is the reason for the increased noise radiation for the minimum vibration case.

The in-plane positions of the retreating side vortex segments (top views of parts (d)-(f)) are not much affected by HHC; the miss distance and the change of miss distance is small (order of 0 - 0.5c), an indication that retreating side BVI is not much changed by the selected MN and MV HHC schedules which is in agreement with the results of the noise directivity measurements (Fig. 12).

LDV RESULTS

Tip Vortex Velocity Field

In Fig. 19 the tip vortex velocity fields measured by the LDV systems are presented. The LDV probe volume was placed at an azimuth angle of about $\psi=55°$ at r/R=0.75 on the adv. side and at $\psi=298°$ and r/R=0.8 on the retr. side. Due to time constraint, only one velocity field on each side (the vortex of most intense BVI) was measured. The adv. side vortex (see Fig. 18) was emitted by blade number 3 (the opposite of the interacting blade) near $\psi=135°$ and was approximately 460° of rotor rotation old; the retreating side vortex was generated by blade number 1 near $\psi=235°$ with an approximate age of 440° at interaction. In parts (a)-(c) of Fig. 19 the resultant U,W velocity vector fields are plotted in the X-Z plane for the three selected cases BL, MN, and MV.

The velocity fields for the BL-case (part (a)) for this nominal BVI condition clearly show the expected vortex structure which appears well focused on the retr. side and quite extended and less focused on the adv. side which was quite surprising. This suggests that the adv. side vortex may have been significantly affected by the multiple (5 or 6) interactions that it has experienced on its way downstream from the emission location near $\psi=135°$, while the retr. side vortex only had two or three interactions (see Fig. 15a). For HHC-MN (part (b)), on the adv. side a vortex-like structure is hardly visible; probably the vortex was displaced too far and therefore out of the measuring range. The retr. side vortex is well defined, but appears to be less intense. For HHC-MV (part (c)), the velocity field clearly indicates a double vortex structure with a clockwise lower and an anti-clockwise upper vortex as seen during the LLS measurements (Fig. 17). The retr. side vortex shape is similar to the BL-case. The formation of two vortices from one blade is due to the negative lift on the blade tip region observed in the second quadrant between $\psi=135°$ and $\psi=150°$ (Fig. 14(c)). At this upstream azimuth location both vortices were emitted side by side (one at the tip, the other one more inboard near the maximum of the spanwise airload gradient). By mutual induction they started to rotate about a common axis when convected downstream, so that the counter-clockwise (more focused) one was observed above the other one. Nothing can be said about the number of turns that may have occurred, unless more detailed LLS and/or LDV measurements have been performed, starting from the location of vortex emission and continued downstream to the BVI encounter.

Vortex Core Size, Vortex Strength, Miss Distance

Important parameters for analytical modelling of rotor wake, tip vortex, and BVI geometry are vortex core dimensions (radius, r_v) and vortex circulation strength, Γ. Both parameters have been determined from the measured velocity fields surrounding and including the vortex of interest.

The vortex core diameter ($d_v=2r_v$) was estimated from the distance between the extrema of curves U/V_T versus Z/c, Fig. 20(a), representing the radial distribution of the normalized axial velocity component across the vortex center at fixed X or from similar curves of normal velocity W/V_T versus X/c at fixed Z (horizontal cut through the vortex center, Fig. 20(b)). The vortex having a priori a trajectory in a quasi horizontal plane, but with its axis not parallel to the Y-axis of the LDV system, is seen by the laser velocimeter in perspective. This effect is minimized when analyzing the data along a vertical axis at fixed X. The vortex core radii shown in Table 1, have been determined in this way, but it is pointed out that the axial velocity distribution (U versus Z) was disturbed in many cases by the wake of the preceding blade and the viscous core diameter was difficult to obtain.

Circulation Γ, representative for vortex strength, is normally computed by integrating velocity components over a closed contour surrounding the vortex core. A constant value of Γ should be obtained when the distance from the vortex core is increased; but this approach was not satisfactory, probably because of the influence of the blade wake which was very close to the vortex and created disturbances in the velocity fields (see Fig. 19). Therefore, circulation has been computed based on previous work of ONERA on delta wings (Ref. 28) using the formula

$$\Gamma=\pi\ /1.2763\cdot\Delta W_{pk-pk}\cdot d_v$$

where ΔW_{pk-pk} is the velocity gap between the extrema of the vortex normal velocity distribution (Fig. 20(b)).

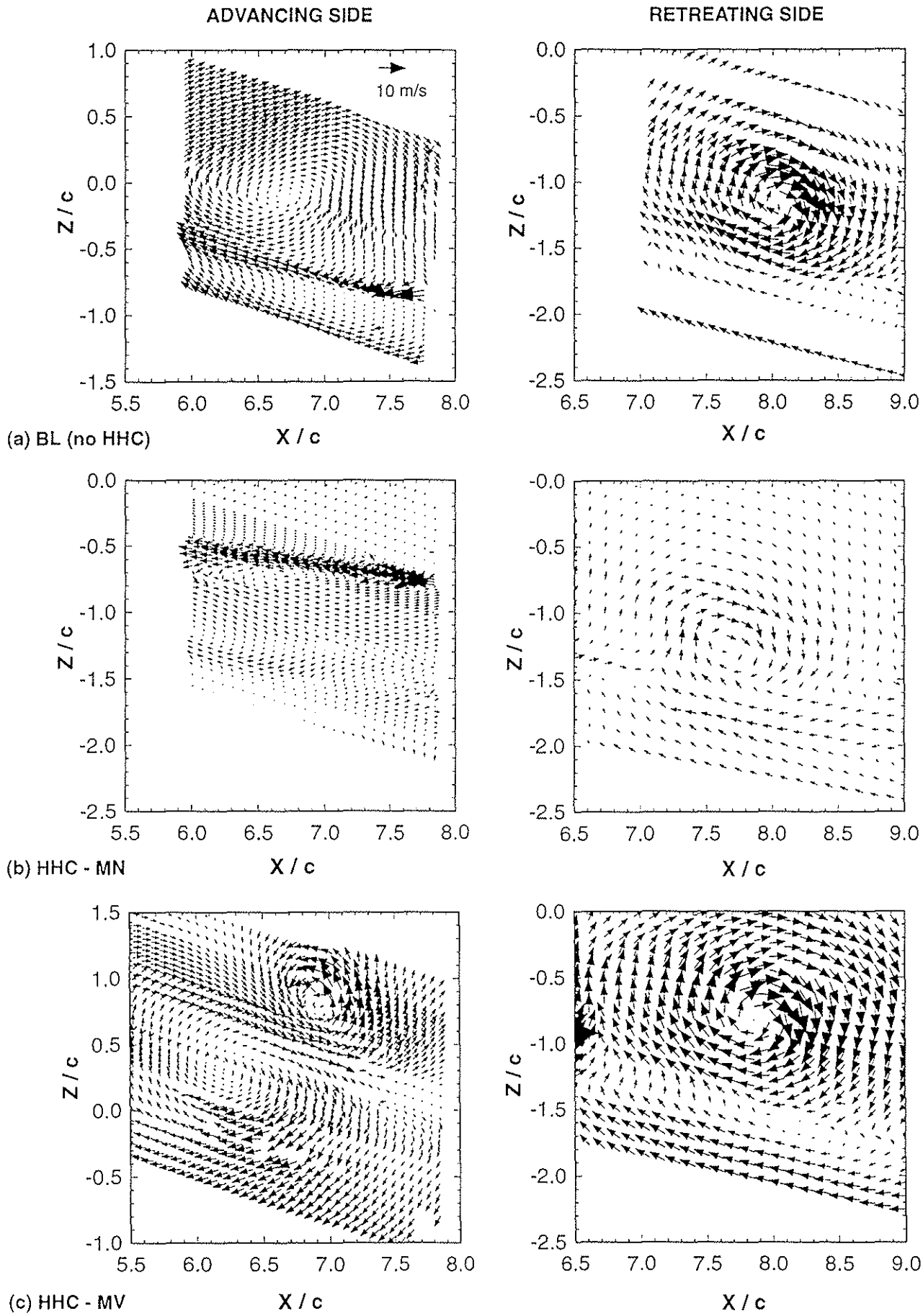

Fig. 19 Tip vortex velocity vector fields (U,W) for BL, MN, and MV cases measured on the adv. side near ψ =54° and on the retr. side near ψ =298°; rotor condition as for Fig. 12.

In addition, the blade-vortex miss distance for each vortex section measured by LDV was determined from the measured vortex core center altitude and the blade tip altitude (measured by TART) at the azimuth locations $\psi = 60°$ and $\psi = 298°$. Since the azimuth angles for the vortex core center and for the blade tip measurement location did not fully agree, the vertical displacement of the vortex core center for the resultant $\Delta\psi$ was calculated assuming a mean convection speed. All measured positions are referenced to the rotor hub position determined by theodolite measurements.

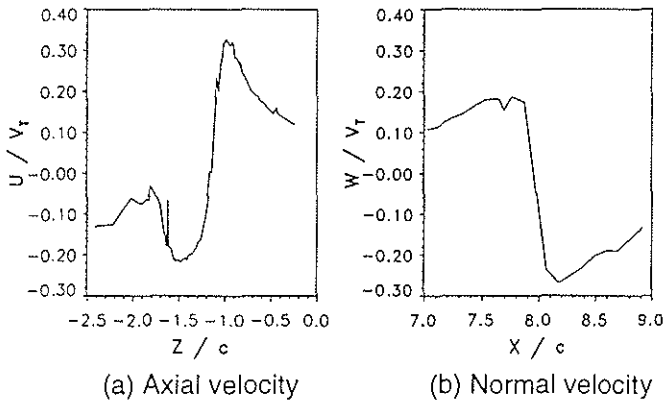

(a) Axial velocity (b) Normal velocity

Fig. 20 Radial velocity distribution through vortex core near $\psi = 298°$ for BL case; rotor condition as for Fig. 12.

The vortex core centers have been determined from the LDV results in various ways taking into account flow characteristics like velocity vector fields (Fig. 19), vorticity fields (maximum at vortex center), longitudinal turbulence profiles ($(u'^2)^{1/2}=f(Z)$; maximum at vortex center), and shear stress profiles ($\overline{u'w'} = f(Z)$; zero at vortex center). From the results of these different analyses a mean value was calculated and used to determine the miss distances on the retr. side, compiled in Table 1. An alternate approach to evaluate the vortex core center position consisted in calculation of the vortex streamlines from the velocity field. In order to obtain closed streamlines surrounding the vortex core, the convection velocity was varied accordingly. The results for the adv. side have been determined using this procedure. Both approaches appear justified. The resultant trends and miss distance values are consistent with those determined by use of the LLS technique (see Fig. 18).

In Table 1 the results are compiled for vortex core radius r_v, vortex strength Γ, and blade-vortex miss distance ΔZ for the investigated descent cases at $\mu = 0.15$ for both adv. and retr. side (neg. ΔZ means vortex below the blade).

BLADE DEFLECTION RESULTS

The results of the blade deflection measurements for the nominal BVI test condition (baseline case and the MN and MV HHC settings) complete the set of parameters important for the BVI problem with regard to the blade-vortex miss distance and the blade loading distribution. Depending on the measurement technique applied the results provide information on the blade deflections either at specific azimuth positions (PGM, TART) or for all azimuth positions within one rotor revolution (strain gauge results).

Spanwise Blade Deflections

In Fig. 21 the elastic flap deflections (part(a)) and the total pitch deflections (part (b)) comprising torsion, twist, and pitch are plotted versus rotor radius. The PGM results are compared to the strain gauge and TART results. The curves represent the deflection difference between the HHC-MN case and the baseline case for the nominal BVI test condition. The comparison of the flap deflections resultant from the three measurement techniques show

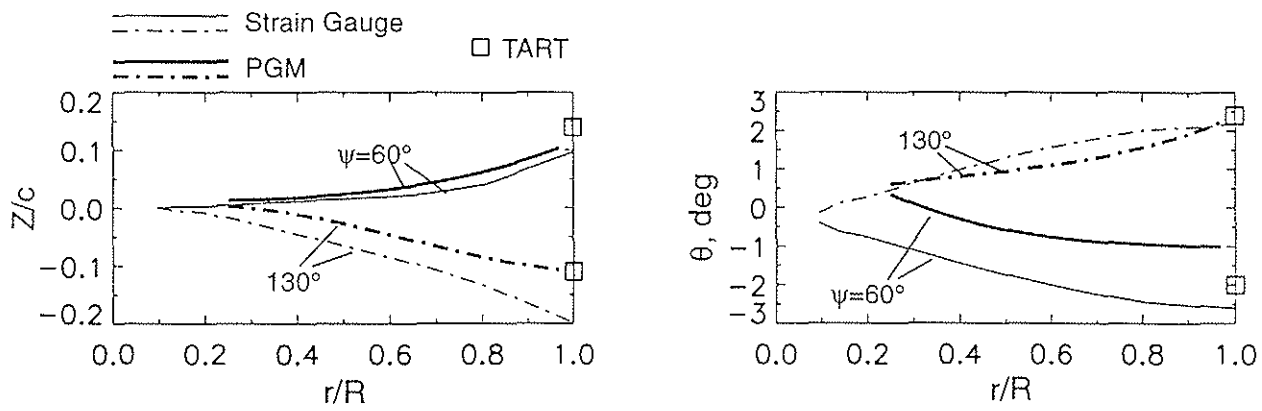

(a) Elastic flap deflection (b) Total pitch deflection

Fig. 21 Spanwise blade deflections (difference between MN and BL) measured with different techniques; rotor condition as for Fig. 12.

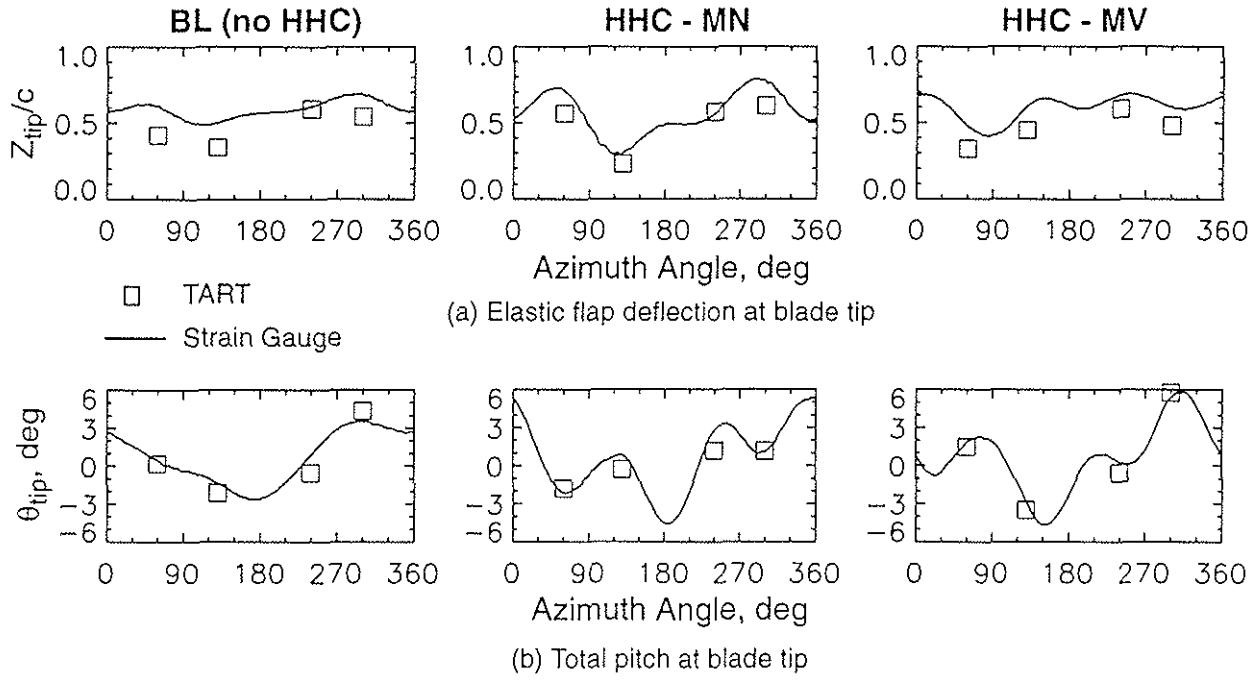

Fig. 22 Blade-tip deflection histories for BL, MN, and MV cases; rotor condition as for Fig. 12.

satisfactory agreement. But the correlation of the PGM results with the strain gauge and TART data for the total pitch deflections is not as good as expected. It appears that the image processing of the PGM video recordings and the subsequent data analysis technique need to be improved to obtain more satisfactory PGM results.

Nevertheless, the flap deflections at the blade tip indicate that the blade tip for the HHC-MN case compared to the baseline case is deflected downward at $\psi=130°$ where the interacting vortices are generated and deflected upward at $\psi=60°$ where BVI occurs, thus contributing to an increase of the blade-vortex miss distance. But this contribution of about 0.25c compared to the total miss distance of about 1.5c determined by LLS (see Fig. 18(a) and (b)) is relatively small; and it can be concluded that the wake deflection due to the additional downwash resultant from the increased blade loading in the second quadrant (Fig. 14(b)) provides the dominant contribution to the blade-vortex miss distance.

Blade-tip Deflections

In Fig. 22 time histories of blade-tip elastic flap deflections (part (a)) and of blade-tip total pitch deflections (part (b)) derived from the strain gauge measurements are provided and compared with TART results. The latter ones were measured at 60° and 300° rotor azimuth near locations where BVI occurred and at 130° and 240° azimuth at regions where the interacting vortices were emitted. As shown in part (b), TART and strain gauge results for the total pitch at the tip agree very well for the baseline case and the HHC-MN and -MV cases. Regarding the flapwise tip deflections (part (a)), the TART and strain gauge results compare reasonably well. The TART results exhibit an average deviation of about 0.1 chord (12mm) toward lower deflection values for all three cases. Whether this offset may be attributed to the TART calibration procedure is still under investigation. In general, the results are consistent with the blade airload distributions of Fig. 14 and the blade-vortex miss distance results shown in Fig. 18. For

Test Condition	r_v/c		Γ (m^2/s)		$\Delta Z/c$	
	adv.	retr.	adv.	retr.	adv.	retr.
BL (α_s=3.8°)	0.38	0.25	1.1	2.3	-0.41	-0.52
BL (α_s=6.8°)	0.38	0.41	1.5	2.6	0.12	0.04
BL (α_s=5.3°)	0.35	0.25	1.4	2.1	-0.04	-0.29
HHC-MN	-	0.42	-	2.2	-	-0.45
HHC-MV (lower vortex)	0.45	0.25	2.2	2.8	0.20	0.12
HHC-MV (upper vortex)	0.27	-	1.6	-	1.21	-

Table 1: Results of the LDV measurements

example, the total pitch history for HHC-MN in Fig. 22(b) is seen reduced in the first quadrant indicating an unloading of the blade, which is consistent with the blade airload reduction illustrated in Fig. 14(b); increased pitch in the second quadrant leads to increased blade loading as confirmed in Fig. 14(b) as well. Furthermore, the flap deflection history in Fig. 22(a) indicates that for the MN case in the first quadrant the blade tip is deflected farther upward compared to the baseline case and displaced more downward in the second quadrant, thus increasing the blade-vortex miss distance at the BVI location and thereby contributing to a reduction of the BVI impulsive noise.

SUMMARY OF KEY RESULTS

In this joint international program a unique set of acoustic, aerodynamic, blade dynamic, rotor wake, performance, and BVI geometry data have been acquired for a number of simulated descent flight conditions without and with HHC activated and systematically varied. In agreement with previous tests a *noise reduction benefit* of approximately 6dB (about 50-percent of the maximum BVI level) was obtained for 3P HHC, 0.85° amplitude, and 38° azimuth control angle (phase angle 296°) termed minimum noise (MN) control. *Vibration reduction* of about 30-percent was accomplished for 3P, 0.85° amplitude, and 119° azimuth control angle (phase angle 177°) termed minimum vibration (MV) control. In general, at maximum noise reduction increased levels for low frequency noise and vibrations were observed, but for a small number of HHC settings both noise and vibrations were noticeably reduced.

Absolute blade surface pressures synchronously measured with rotor performance and acoustic data have been acquired for HHC rotor operation for the first time. Actual in-plane BVI locations have been determined from the (near) leading edge blade pressure histories.

Sectional airload or lift distributions, calculated from the blade surface pressures, were found to be extremely useful for a better understanding of the physics behind the effects of multicyclic pitch variation on noise and vibration. Since directly influenced by HHC, *local airload* represents a *primary parameter* for the related change of BVI noise and vibration because:
(1) it determines local tip vortex strength at azimuth of vortex formation and blade unloading (pitch reduction) at azimuth of blade-vortex interaction,
(2) it controls via its induced velocity field in the blade wake (up- or downwash due to negative or positive loading) the tip vortex convection normal to the rotor plane,
(3) it affects the torsional and especially the flapwise blade deflection, and
(4) it strongly influences the BVI geometry in general and blade-vortex miss distance in particular by the combined effects of the features of statements (2) and (3). It was found that flapwise blade deflection contributes relatively little (about 10-20-percent) to the total miss distance determined for the MN HHC case,
(5) it also controls the rotor vibrations by the combined effect of the low frequency part of the airload and the dynamic blade response. By proper phasing of the airloads the excitation of blade oscillations can be distinctly suppressed, and
(6) it finally determines the vortex formation (roll-up) and structure as was seen by the double vortex structure of the MV HHC case due to negative lift on the blade tip at the azimuth of vortex emission.
Very valuable information on BVI geometry, vortex strength, and core size was obtained from the flow visualization and non-intrusive flow field measurements by LLS and LDV and on elastic blade deflections from application of PGM and TART.

From the *LLS technique* qualitative images of the tip vortex structure (e.g. double vortex) were attained and quantitative information on *tip-vortex geometry segments* and its *miss distance* to the blade near the azimuth of interaction.

By *LDV applications* the velocity fields of the tip vortices (one on each the adv. and retr. side) generating most intense BVI were determined. More insight into the vortex structure was gained and the double vortex system for the MV HHC case verified. *Vortex strength* (circulation) of the interacting vortex was found consistent with previous results (Ref. 29) confirming a structured distribution within the vortex, but showed only limited effect on BVI noise in this test. The retr. side values were significantly higher than on the adv. side, but they did not change much with HHC application.

Vortex core radius was determined and seen 50-percent larger on the adv. side compared to the retr. side for the baseline descent cases investigated; probably an effect of the multiple BVI experienced by the advancing side vortices. For MN control settings the core size was increased on the retreating side by about 70-percent (while core size on adv. side could not be determined).

Elastic blade deflections attained along the blade span by *PGM* and *strain gauge measurements* and at the tip by the *TART method*, clearly showed that the miss distance was increased for minimum noise blade pitch control and decreased for minimum vibration.

CONCLUDING REMARKS

In conclusion, the narrowly defined technical objectives have been fully satisfied. For a number of descent conditions known to generate BVI a high quality data base of simultaneous aerodynamic blade pressure and acoustic

data without and with HHC application was established. For a few typical BVI baseline conditions and two special HHC schedules for minimum noise and minimum vibration supplementary information on the rotor wake, aeroelastic blade deformation, and the BVI geometry was obtained. From the basic parameters expected to contribute to BVI noise reduction, blade-vortex miss distance was shown to be the most important parameter that needs to be increased, followed by unloading the blade at interaction, while vortex strength was found to be increased. The miss distance itself was dominated by aerodynamically induced tip vortex convection rather than by flapwise blade displacements at vortex emission and blade-vortex interaction locations. All of these parameters are controlled by local blade airload, which represents the key parameter for noise and vibration reduction by HHC.

The results are expected to contribute to further improvement of the wake prediction codes by implementing multi-vortex roll-up modelling considered necessary for more accurate prediction of the BVI geometry and blade vortex miss distance. For code validation the rather complete aerodynamic and acoustic data base will be sufficient, however, some more specific information may be required on the tip vortex evolution from emission to interaction including roll-up, downstream convection, vortex aging, and eventually vortex bursting, to more completely understand the BVI problem.

ACKNOWLEDGEMENT

In a test of such complexity there are many people who deserve recognition for a job professionally and well done. The authors would like to thank the engineers, technicians and mechanics of DLR, ONERA, and DNW for their individual motivation and performance. The thanks is extended to the research personnel and to the managers of the research organizations in the four countries (US, France, The Netherlands, and Germany); their devotion to jointly achieve this challenging goal set an example for future cooperative research initiatives.

REFERENCES

[1] Schmitz, F.H.; Boxwell, D.A.: "In-flight Far-field Measurement of Helicopter Impulsive Noise", Journal of the American Helicopter Society, Vol. 21, No. 4, 1976.

[2] Boxwell, D.A.; Schmitz, F.H.: "Full-scale Measurements of Blade/vortex Interaction Noise", Journal of the American Helicopter Society, Vol. 27, No. 4, 1982.

[3] Cox, C.R.: "Helicopter Rotor Aerodynamic and Aeroacoustic Environments", AIAA 77-1338, 1977.

[4] Schlinker, R.H.; Amiet, R.K.: "Rotor-vortex Interaction Noise", NASA CR 3744, 1983.

[5] Splettstoesser, W.R.; Schultz, K.J.; Boxwell, D.A.; Schmitz, F.H.: "Helicopter Model Rotor Blade/vortex Interaction Impulsive Noise: Scalability and Parametric Variations", NASA TM 86007, 1984.

[6] Martin, R.M.; Splettstoesser, W.R.; Elliott, J.W.; Schultz, K.J.: "Advancing Side Directivity and Retreating Side Interactions of Model Rotor Blade-vortex Interaction Noise", NASA TP 2784, AVSCOM TR 87-B3, 1988.

[7] Hoad, D.R.: "Helicopter Blade-vortex Interaction Locations: Scale-model Acoustics and Free-wake Analysis Results", NASA TP 2658, 1987.

[8] Splettstoesser, W.R.; Schultz, K.J.; Martin, R.M.: "Rotor Blade-vortex Interaction Impulsive Noise Source Identification and Correlation with Wake Predictions", AIAA-87-2744, 1987.

[9] Lehmann, G.; Kube, R.: "Automatic Vibration Reduction at a Four Bladed Hingeless Model Rotor - A Wind Tunnel Demonstration", Paper 60, Proceedings 14th European Rotorcraft Forum, Milano, Italy, 1988.

[10] Hardin, J.C.; Lamkin, S.L.: "Concepts for Reduction of Blade-vortex Interaction Noise", AIAA-86-1855, 1986.

[11] Splettstoesser, W.R.; Lehmann, G.; van der Wall, B.: "Higher Harmonic Control of a Helicopter Rotor to Reduce Blade-vortex Interaction Noise", Z.F.W. (Zeitschrift für Flugwissenschaften), Vol. 14, pp. 109-116, 1990. (See also Proceedings of the 15th European Rotorcraft Forum, Sept. 1989.)

[12] Polychroniadis, M.: "Generalized Higher Harmonic Control, Ten Years of Aerospatiale Experience", Paper III 7.2, Proceedings 16th European Rotorcraft Forum, Glasgow, UK, 1990.

[13] Brooks, T.F.; Booth, E.R.; Jolly, J.R.; Yeager, W.T.; Wilbur, M.L.: "Reduction of Blade-vortex Interaction Noise Through Higher Harmonic Pitch Control", Journal of the American Helicopter Society, Vol. 35, No. 1, Jan. 1990. (See also NASA TN-101624/AVSCOM TM 89-B-005, July 1989.)

[14] Brooks, T.F.; Booth, E.R.; Boyd, D.D.; Splettstoesser, W.R.; Schultz, K.J.; Kube, R.; Niesl, G.H.; Streby, O.: "HHC Study in the DNW to Reduce BVI Noise - An Analysis", Proceedings AHS/RAeS International Technical Specialists' Meeting - Rotorcraft Acoustics and Fluid Dynamics, Philadelphia, PA, Oct. 1991.

[15] Splettstoesser, W.R.; Schultz, K.J.; Kube, R.; Brooks, T.F.; Booth, E.R.; Niesl, G.; Streby, O.: "A Higher Harmonic Control Test in the DNW to Reduce Impulsive BVI Noise", Journal of the American Helicopter Society, Vol. 39, No. 4, Oct. 1994. (See also Proceedings 17th European Rotorcraft Forum, Berlin, Germany, 1991.)

[16] Yu, Y.H.; Gmelin, B.; Heller, H.; Phillipe, J.J.; Mercker, E.; Preisser, J.S.: "HHC Aeroacoustic Rotor Test at the DNW - The Joint German/French/US Project", Proceedings 20th European Rotorcraft Forum, Amsterdam, The Netherlands, 1994.

[17] Gmelin, B.L.; Heller, H.H.; Mercker, E.; Philippe, J.J.; Preisser, J.S.; Yu, Y.H.: "The HART Programme, a Quadrilateral Cooperative Research Effort", Proceedings American Helicopter Society 51st Annual Forum, Ft. Worth, TX, May 1995.

[18] Beaumier, P.; Prieur, J.; Rahier, G.; Spiegel, P.; Demargne, A.; Kube, R.; van der Wall, B.G.; Schultz, K.J.; Splettstoesser, W.; Tung, C.; Gallman, J.; Yu, Y.H.; Brooks, T.F.; Burley, C.L.; Boyd, D.D.: "Effect of Higher Harmonic Control on Helicopter Rotor Blade-vortex Interaction Noise: Prediction and Initial Validation", 75th Fluid Dynamics Panel Symposium on Aerodynamics and Aeroacoustics of Rotorcraft, Berlin, October 10-13, 1994.

[19] Boutier, A.; Lefèvre, J.; Soulevant, D.; Dunand, F.: "2D Laser Velocimetry Near Helicopter Blades in DNW (NLR)", in ICIASF '93 Record, pp. 32.1-32.8, 1993.

[20] Seelhorst, U.; Bütefisch, K.A.; Sauerland, K.H.: "Three Component Laser-Doppler-Velocimeter Development for Large Wind Tunnel", in ICIASF '93 Record, pp. 33.1-33.7, 1993.

[21] Splettstoesser, W.R.; Junker, B.; Schultz, K.J.; Wagner, W.; Weitemeier, W.; Protopsaltis, A.; Fertis, D.: "The HELINOISE Aeroacoustic Rotor Test in the DNW - Test Documentation and Representative Results", DLR-Mitteilung 93-09, 1993 (in English).

[22] Mercker, E.; Pengel, K.: "Flow Visualization of Helicopter Blade Tip Vortices - A Qualitative Technique to Determine the Trajectory and the Position of the Tip Vortex Pattern of a Model Rotor", Proceedings 18th European Rotorcraft Forum, Avignon, France 1992.

[23] Brooks, T.F.; Jolly, J.R.; Marcolini, M.A.: "Helicopter Main Rotor Noise-Determination of Source Contributions Using Scaled Model Data", NASA TP-2825, Aug. 1988.

[24] Kube, R.; Splettstoesser, W.R.; Wagner, W.; Seelhorst, U.; Yu, Y.H.; Boutier, A.; Micheli, F.; Mercker, W.: "Initial Results from the Higher Harmonic Control Aeroacoustic Rotor Test (HART) in the German-Dutch Wind Tunnel", 75th Fluid Dynamics Panel Symposium on Aerodynamics and Aeroacoustics of Rotorcraft, Berlin, October 10-13, 1994.

[25] Caradonna, F.X.; Laub, G.H.; Tung, C.: "An Experimental Investigation of the Parallel Blade-vortex Interaction", Proceedings 10th European Rotorcraft Forum, The Hague, The Netherlands, Aug. 1984.

[26] Beaumier, P.; Spiegel, P.: "Validation of ONERA Prediction Methods for Blade-vortex Interaction Using HART Results", Proceedings American Helicopter Society 51st Annual Forum, Ft. Worth, TX, May 1995.

[27] Tung, C.; Gallman, J.M.; Kube, R.; Wagner, W.; van der Wall, B.; Brooks, T.F.; Burley, C.L.; Boyd, D.D.; Rahier, G.; Beaumier, P.: " Prediction and Measurement of Blade-vortex Interaction Loading", Proceedings 1st Joint CEAS/AIAA Aeroacoustics Conference, Munich, June 1995.

[28] Batchelor,: "Fluid Dynamics", Cambridge University Press, 1972.

[29] Tung, C.; Pucci S.L.; Caradonna, F.X.; Morse, H.A.: "The Structure of Trailing Vortices Generated by Model Rotor Blades", Vertica Vol. 7, No. 1, pp. 33-43, 1983.